MSc Physics and Astronomy

Advanced Matter and Energy Physics

$CsPbBr_3$ nanocubes as seed-layer for epitaxial thin-film growth of perovskite

---

by

Daan Methorst

10722688

Master Thesis

60 ECTS

September 2021 - July 2022

Supervisors:

prof. dr. E.C. (Erik) Garnett & prof. dr. P. (Peter) Schall

Abstract

Lead halide perovskites are a promising material for photovoltaic applications. The crystal structure of a lead halide perovskite has an influence on the properties of the material. Different methods could be used to fabricate lead halide perovskite thin-films. The method used for fabrication has a large impact on the crystal structure of the thin-film. With conventional fabrication methods, like spincoating, the thin-film contains a large number of grains with a big angle of misorientation between them. In this thesis, a new method of fabrication of lead halide perovskite thin-film is investigated in an attempt to create a well-oriented thin-film. Assembled $CsPbBr_3$ nanocubes are used as a seed-layer for overgrowth of $Ch_3NH_3PbI_3$ (MAPI) thin-film deposited by chemical vapour deposition (CVD). The effect of separate parameters for CVD is investigated to achieve a fully covered MAPI thin-film. The used method results in a MAPI thin-film with a significantly lower angle of misorientation between neighbouring grains compared to a spincoated MAPI thin-film. The agreement in orientation is most likely due to the nanocube seed-layer which acts as a template for the crystal growth.

Contents

1 Introduction

Controlling climate change is one of the biggest challenges of the 21st century. According to the latest agreements, the world needs to be CO_2 neutral by 2050 and afterwards, capture even more CO_2 from the atmosphere than emitted.[1] A huge transition in energy usage worldwide is needed to satisfy this agreement.[2] Photovoltaics (PV) could be a key player in this energy transition because the transition from photons to electric energy with the use of photovoltaic devices doesn't generate excess CO_2.[3] But, while the creation of electric current from solar energy doesn't 'cost' emitted CO_2, the creation of these, mainly silicon, solar panels 'costs' a lot of CO_2.[4] Silicon solar modules are the dominating technology for PV worldwide. Silicon-based PV technology accounted for about 95% of the total production in 2020.[5] To fabricate silicon solar cells, silicon is extracted from the ground and converted into monocrystalline silicon by an extremely energy-intensive process. The energy payback time to compensate for the emitted CO_2 during the fabrication is 1.2 years, considering the PV module is installed in Northern Europe.[5] To decrease the energy payback time it is needed to improve the fabrication method of photovoltaic devices.

Perovskites are a great alternative to silicon for photovoltaic applications. Perovskite solar cells (PSCs) are easy to fabricate by a solution method.[6] The production is very low-cost compared to the production of traditional silicon photovoltaic devices and can be achieved by utilizing fewer materials.[6] PSCs have already shown similar power convergence efficiency (PCE) as silicon solar cells.[7] The biggest challenge to overcome for these PSCs, however, is the stability of the devices. While silicon solar cells degrade in a matter of decades, PSCs are known to degrade in days, if not hours.[8] To understand PSCs, it is of great importance to understand the crystal structure and the effect it has on the properties of the perovskite. There is a substantial debate on the effect of the crystal structure on the properties of the cell.[9] To help settle this debate, it is of great importance to compare thin-films with different crystal structures. To fabricate different thin-films, different methods of fabrication should be investigated.

In this thesis, a new method is investigated that attempts to control the orientation of grains in a perovskite thin-film. First, in section 2 the theory behind the research is explained. Next, in section 3, the methods of the experiment are shown, followed by an explanation of the characterization of the produced samples. In section 4 the results of the research will be shown and finally, in section 5, the results will be summarized and concluded and an outlook for future research will be given.

2 Theory

In this section, the theoretical background of the research is explained. First, a review considering lead halide perovskites and their semiconducting properties is given in section 2.1. Second, an introduction to carriers in lead halide perovskite is given in section 2.2, followed by an explanation of the crystallisation and epitaxial growth of thin film perovskites in section 2.3. Finally, this section will conclude with insights into lead halide perovskite nanocubes.

2.1 Lead Halide Perovskite

Perovskites are a collection of materials which are made of the same crystalline structure, described by the chemical formula ABX_3.[11] In this structural formula the A and B represent cations and the X represents anions. The atoms in this structure typically form a cubic structure, which is shown in figure 1. The A site forms the centre of the cubic structure of the B sites. The X atoms form octahedra around the B atoms. The unit cell shown in figure 1 repeats itself to form a crystal. In halide perovskites, the X site is occupied by a halide (Cl-, Br-, I-). In inorganic halide perovskites, the A site is occupied by an inorganic ion, caesium for example, while in organic halide perovskites, the A site is occupied by an organic ion. In this research, work is done on both inorganic and organic lead halide perovskites namely, $CsPbBr_3$ and $CH_3NH_3PbI_3$ (MAPI).

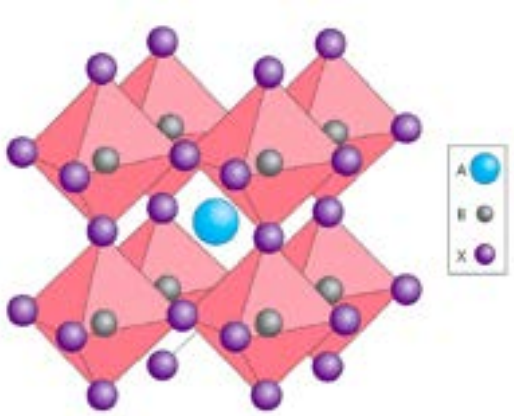

Figure 1: *Perovskite unit cell. Figure obtained from Anita and Snaith.*[10]

2.1.1 Lead halide perovskites as semiconductors

Lead halide perovskites exhibit semiconducting properties.[11] Typically, in a semiconducting crystal, the electrons in the outermost shell of the atoms interact with the outermost electrons of other atoms.[3] Covalent bonds are formed between neighbouring outer electrons. At 0 K (no energy added), the bonds can be visualized by the bonding model, which is schematically shown in figure 2a. But, when energy is added to the system, bonds between electrons can be broken, resulting in 'freeing' electrons from their covalent bonds, forming a free electron. The site where the electron used to be is now positively charged and is called a hole. This

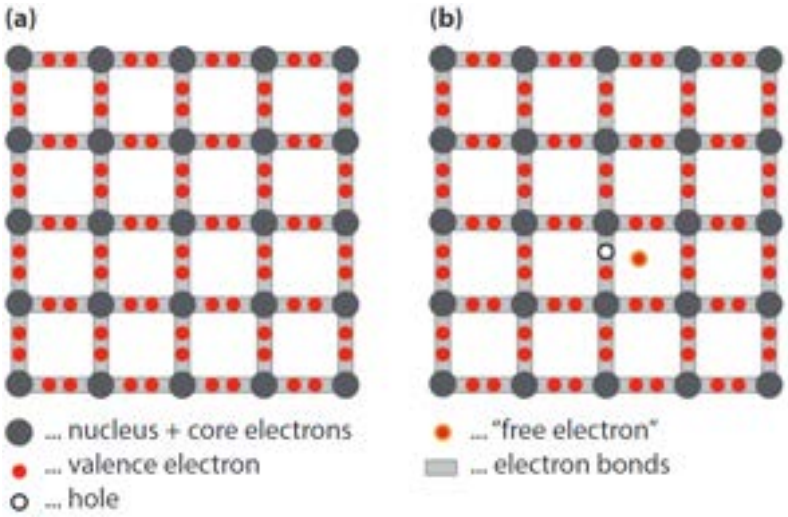

Figure 2: *Schematics of the bonding model. (a) The electronic bonds aren't broken. (b) One bond between the atoms is broken, which results in a free electron and a hole. Figure obtained from Smets et al.*[3]

process is seen in figure 2b in a simplified manner. When a free electron-hole pair is formed, a neighbouring electron can now occupy the hole next to it, resulting in movement of the hole.

The periodic structure of semiconductors results in allowed energy states electrons can occupy and states that are not allowed, resulting in a 'forbidden' bandgap. The energy states allowed for valence electrons form the valence band and the energy states allowed for excited free electrons form the conduction band. The bandgap separates the two bands.

For electrons in the valence band to be excited to the conduction band, it is needed to overcome this bandgap. The energy needed for this can be obtained from a photon. A photon carrying enough energy can excite an electron from the valence band to the conduction band, leaving a hole. The created excited electrons and holes are called carriers.

2.2 Carrier recombination

Created carriers will decay over time. This is a consequence of the recombination of the created electron and hole. There are three basic types of recombination: radiative recombination, trapstate-assisted recombination and Auger recombination.[12] Radiative recombination is the recombination of an excited electron back to a hole in the valence band, by emitting a photon corresponding to the bandgap energy.[13] Trapstate-assisted recombination is facilitated by lattice defects or impurities in the crystal.[14] The recombination does not occur band to band, but the excited electron falls back to a trap state with an energy within the forbidden gap. Recombination with a hole is then the next step. In this process, the energy is lost to vibrations in the lattice, which is then dissipated as heat. This process is therefore called non-radiative. Trap-state assisted recombination is in MAPI thin-films often the most dominant recombination form.[15] Auger recombination is also a non-radiative process. It involves 3 particles, namely 2 electrons and 1 hole or the other way around. In the example of two electrons, one electron in the conduction band recombines with a hole in the valence band. The energy 'won' is not released in radiation but is absorbed by an already excited electron in the conduction band. The electron moves to a higher energy state. This energy is then lost to vibrations in the lattice until it has fallen back to the conduction band edge. Auger recombination, therefore, strongly depends on the charge carrier density.[16] For solar cells, it is of great importance to create a crystal where carriers experience a long lifetime, so electrons and holes can be extracted by the anode and cathode before they recombine.[17] To reduce recombination, one could, for example, minimize the lattice defects to reduce trapstate-assisted recombination.

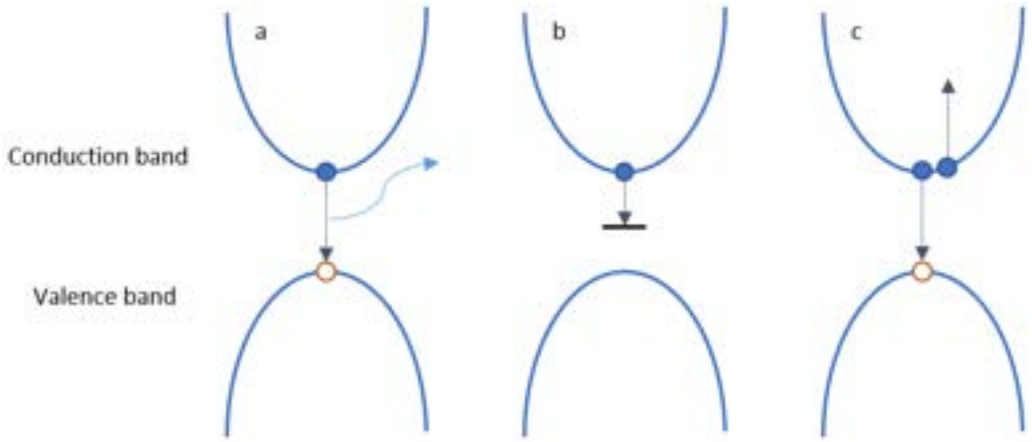

Figure 3: *Different recombination processes. (a) Radiative recombination: A photon is emitted when the electron and hole recombine. (b) Trapstate-assisted recombination: a excited electron falls into a trapstate. Excess energy is lost to lattice vibrations. (c) Auger recombination: Energy of an excited electron is obtained by an electron already in the conduction band.*

2.3 Crystal growth and grains

As previous stated, trap-states are formed by impurities of the lattice. Grain boundaries are by definition sites where neighbouring crystal lattices don't match. Hence, at grain boundaries, the trap-state density is rather high.[19]

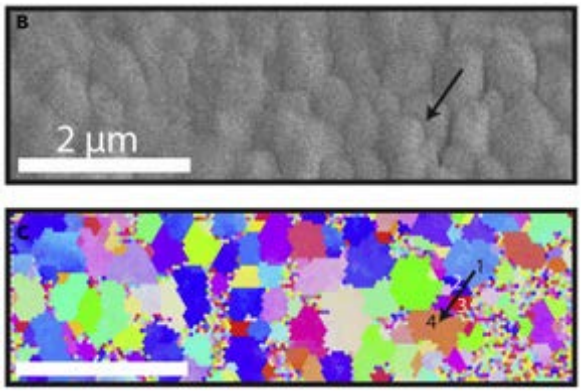

Figure 4: *Image made by EBSD to demonstrate the presence of multiple grains in a film. Figure obtained from Jariwala et al.*[18]

To reduce the density of defects in a film, it is useful to create a film with large crystal grains, which have a small angle of misorientation. A crystal grain or a crystallite is a smaller crystal in the bulk of the material. Different grains are distinguishable by the different orientations of the crystal lattice in the grains. In a film, multiple different grains can be formed from growth from different nucleation sites.[20] From the nucleation sites the crystal grains grow bigger and eventually meet, forming grain boundaries.[19] Figure 4 shows the surface of a crystal film where different grains are easy to observe. The different orientations of the crystal lattice in the grains give rise to vacancies, misplaced atoms and dislocations and other defects or traps at the grain boundaries.

A material could be built from lots of grains; such a material is called polycrystalline. As stated in the previous section it is for traditional semiconductors beneficial to contain an active layer with as few defects as possible. Because grain boundaries are regions with crystal defects, a single-crystal is favourable. For perovskites, however, there is no agreement on the effects of having a high or low grain density. Perovskites are known for being very defect-tolerant.[21] Grain boundaries could even have a positive effect on the properties of large crystal MAPI thin-films because they would act as walls for charge carries which slows down their carrier decay time.[22] However, substantial research has also been done proving grain boundaries negatively affect the electronic properties of the film. For example, increasing the grain size of MAPI by post-annealing leads to an enhancement of photoluminescence and an increase in carrier lifetime.[23] Furthermore, a high density of grain boundaries could also decrease the stability of the perovskite, because they could act as a channel for oxidation.[24] Still, more research is needed to prove the effect of grains and their boundaries on the overall performance of perovskite solar cells. To investigate this, new methods to fabricate perovskite thin-films with high or low grain density with different angles of misorientation are needed. In this research, a method to fabricate thin film perovskite with low grain density and low angle of misorientation is investigated.

2.4 Fabrication and template-assisted overgrowth

Different techniques are used to fabricate thin-film perovskite. Thin-films are made via spincoating, dipcoating, dropcasting, inkjet printing and various vapour deposition techniques.[13] Spincoating is one of the most used techniques to create a thin-film perovskite.[25] First a solution containing the precursors of the perovskite dissolved in a solvent is dropcasted onto a substrate. For MAPI the precursors are CH_3NH_3I (MAI) and PbI_2. The substrate is then rotated fast so the liquid spreads over the full surface of the sample. The speed of rotation also causes the liquid to flatten out. Then, while rotating, an antisolvent is dropcasted onto the substrate. Adding the antisolvent crystallises the precursors into a perovskite thin-film. The sample is then transferred onto a hotplate so the residual solution can evaporate. Schematics of this process are shown in figure 5.

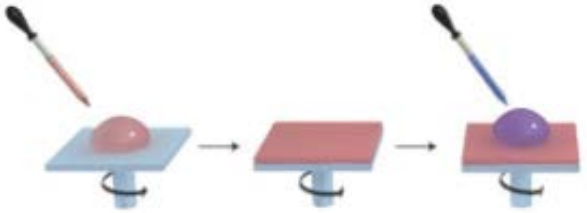

Figure 5: *Schematic display of how a spincoat process would look like. Figure obtained from Mitzy et al.*[19]

By spincoating however, a lot of different nucleation sites are formed and a high amount of small grains are formed. Figure 6 shows the misorientation between grains in a MAPI film fabricated by spincoating. Neighbouring grains show to have a misorientation ranging from $0°$ to $90°$. Some neighbouring grains even show a misorientation of $45°$ which is for cubic lattices the highest angle of misorientation possible. This results in a high lattice defect density at the boundaries. By post-annealing, the perovskite crystal structure reforms to some bigger grains, but the perovskite thin-film is far from single crystalline.[23]

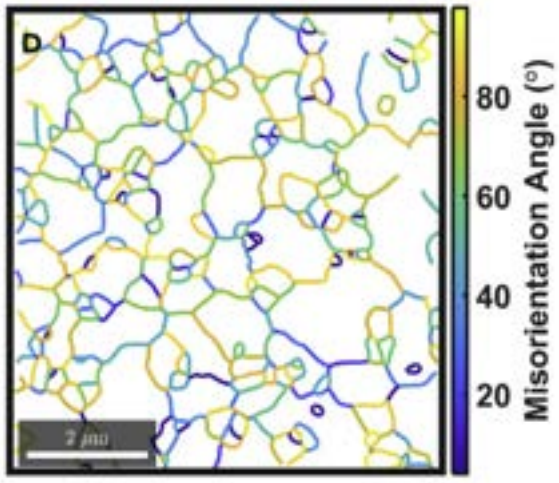

Figure 6: *Map of a spincoated MAPI film which shows different grains and the angle of misorientation at the boundaries between the grains. Figure obtained from Jariwala et al.*[18]

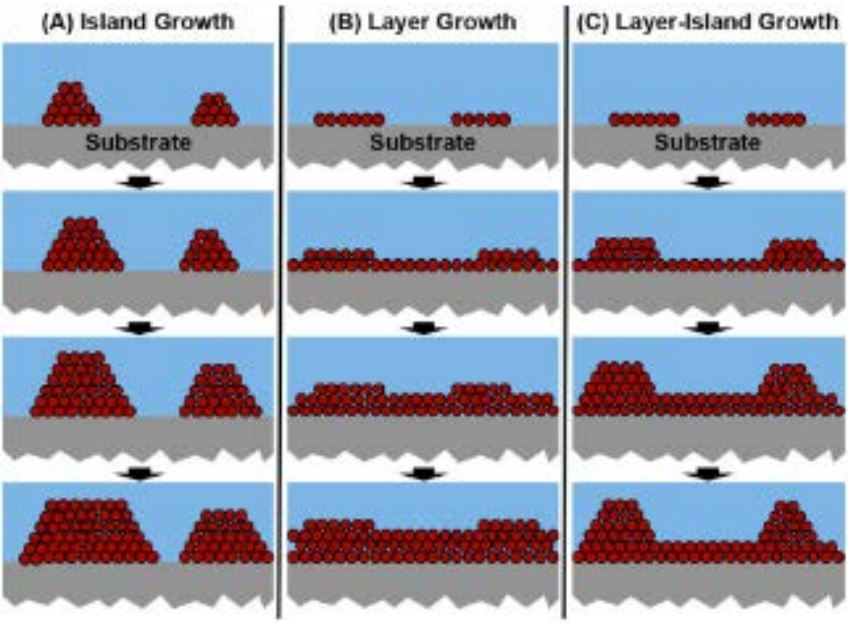

Figure 7: *Schematic view of different growth modes with;(A) Volmer-Weber, (B) Frank-van der Merwe and (C) Stranski-Krastanov. Figure obtained from Mitzy et al.*[19]

Another technique used for thin-film crystal growth is chemical vapour deposition (CVD). The CVD method makes use of a vacuum, a gasflow and a temperature gradient to deposit a film onto a substrate.[26] A further explanation of the process is given in section 3.1.5. Because the deposited material immediately crystallises on the substrate, with this technique the surface of the substrate underneath is of high influence. The substrate could act as a template for the growth of the deposited crystal. If the lattice parameters of the crystal structure of both the substrate and the deposited film have a low mismatch, the thinfilm growth could even be epitaxial. The term epitaxy literally means 'arrangement on' and is used for crystal growth that follows the exact orientation of the substrate.[27] The lattice mismatch is calculated by the following equation:

$$\epsilon = \frac{\alpha_f - \alpha_s}{\alpha_f} \times 100 = ...\%$$

Here, ϵ is the lattice mismatch in percentage and α_f and α_s are the lattice parameters of the film and substrate, respectively. For epitaxial growth to occur the lattice mismatch should be close to 0%. A lattice mismatch of 5%. could already prevent epitaxy.[27]

For epitaxial growth, three different growing modes are classified. These growing modes are called; Volmer–Weber (VW), Frank–van der Merwe (FM) and Stranski–Krastanov (SK).[19] A schematic view of the three modes is seen in figure 7. The difference between these modes is caused by the attractive force between adsorbate-adsorbate and adsorbate-surface. The growth of the film will follow the mode which minimizes the surface energy.

For the Volmer-Weber growth mode, the adsorbate-adsorbate attractive interactions are stronger than the adsorbate-surface interactions. Atoms favour to be deposited onto the

already crystallised adsorbates, because this minimizes the surface energy. Islands are formed by local nucleation on the substrate. The epitaxially grown layer is formed when the islands expand and meet.[28] For the Frank-van der Merwe growth mode, both interactions are balanced. The film growth takes place layer by layer. The surface energy is minimized when the absorbate grows on top of the surface as a single crystal thin-film.[28] The Stranski-Krastanov mode is a combination of the two modes above. First, the growth develops layer by layer, but because of a small lattice mismatch, the strain energy increases when the film grows thicker. Eventually, the strain energy reaches a certain point where the energy is released by the nucleation of separate crystalline islands. This critical thickness is defined by the lattice mismatch and the strain resulting from the layers built on top of the substrate.[28] Previous mentioned growing modes are only possible when the lattice parameters have a small mismatch. If not, multiple grains will form from multiple nucleation sites, just like a spincoated crystal film. But when the mismatch is low, or when a multiple of the lattice parameters fit together, an almost perfect single crystal thin-film could epitaxially grow from the substrate. Research has shown that $CsPbBr_3$ can grow to form a single-crystal thin film when deposited by a vapour method onto $SrTiO_3$.[29] According to this research 2x2 unit cells of $CsPbBr_3$ overlap with 3x3 unit cells of $SrTiO_3$, hence a single-crystal film is grown upon the substrate. Figure 8 shows a snapshot of what the crystal growth during this process looks like.

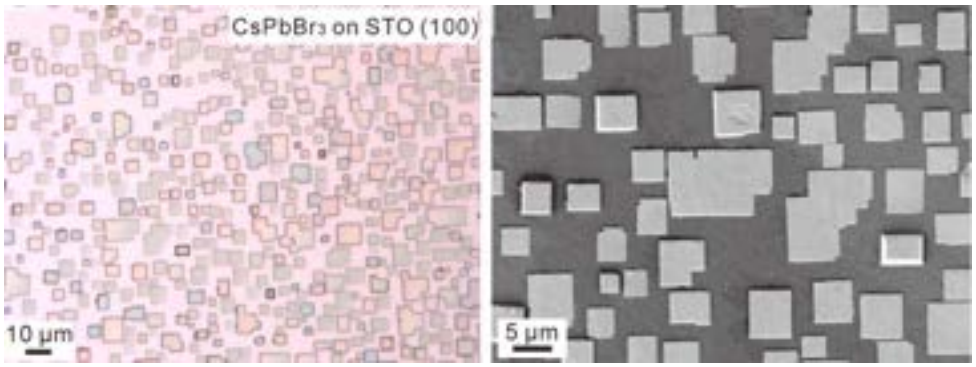

Figure 8: *Snapshot of $CsPbBr_3$ epitaxially grown onto $SrTiO_3$ Figure obtained from Chen et al.*[29]

According to previous research, it is clear that epitaxial growth is an excellent method to grow a thin-film with low defects and a low grain density.[27] It is also clear that for epitaxial crystal growth, lattice parameters should match. However, for most perovskite devices such as LEDs and solar cells, materials are used without an agreement in lattice parameters, e.g. the lattice parameters of cubic-phase MAPI at room temperature and single crystal silicon are 0.630 nm and 0.543 nm, respectively.[30][31] Given these lattice parameters, the calculated lattice mismatch is $\approx 13.8\%$. Moreover, other materials often used in devices, like FTO and ITO, are too polycrystalline to be used as substrates for epitaxial overgrowth. Thus, it would be interesting to find a method that does make it possible to grow a thin-film of well-oriented perovskite on top of previously mentioned substrates that normally wouldn't apply for epitaxy.

In this research, a new method to grow perovskite epitaxially is investigated. In between

the substrate and film a thin layer of assembled nanocubes is added. The layer of assembled nanocubes will act as a template to assist a well-oriented growth of MAPI thin film. The nanocrystals will share a smaller lattice mismatch with the crystal lattice of the grown MAPI than silicon. The crystal lattice constant of the used nanocubes is 0.587 nm.[32] The lattice mismatch when using these nanocubes is now $\approx 6.8\%$. This is still a rather large lattice mismatch for epitaxy to occur, but the flexibility of perovskites could result in a relatively low strain energy, which could make epitaxy feasible.

2.5 Nanocubes as seed layer

In order to enable oriented growth of perovskite on substrates used for devices, nanocubes could be used as a seed-layer for template-assisted overgrowth. A perovskite nanocube is a single-crystal perovskite shaped like a cube. By definition, the size of a nanocube is in the nanometer regime. It's capped by ligands, usually made from organic carbon chains.[33] These ligands prevent the cubes from merging together when formed. Figure 9 shows the schematics of a nanocube. In section 3.1.2 the synthesis of $CsPbBr_3$ nanocubes is demonstrated. Research by Patra et al. has shown that $CsPbBr_3$ nanocubes in solution can be used for self-assembly into a closed-packed monolayer of nanocubes.[32] After self-assembly these cubes are aligned, as seen in figure 10. Similar to hetero-epitaxy, explained in the previous section, the self-assembly of nanocubes is also dependent on the interface energy between the surfaces of the nanocubes and the solvent. A requirement for self-assembly in a monolayer is that the wettability of solvent and surface has to be good. This means that surface energy is minimized if the solvent spreads over the whole surface. So when the solvent is evaporated, the cubes are all assembled in a closed-packed monolayer.

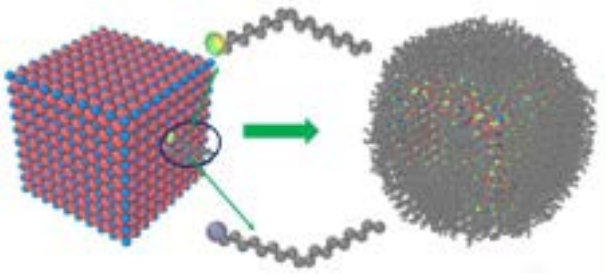

Figure 9: *Schematic view of nanocube with capping ligands. Figure obtained from Patra et al.*[32]

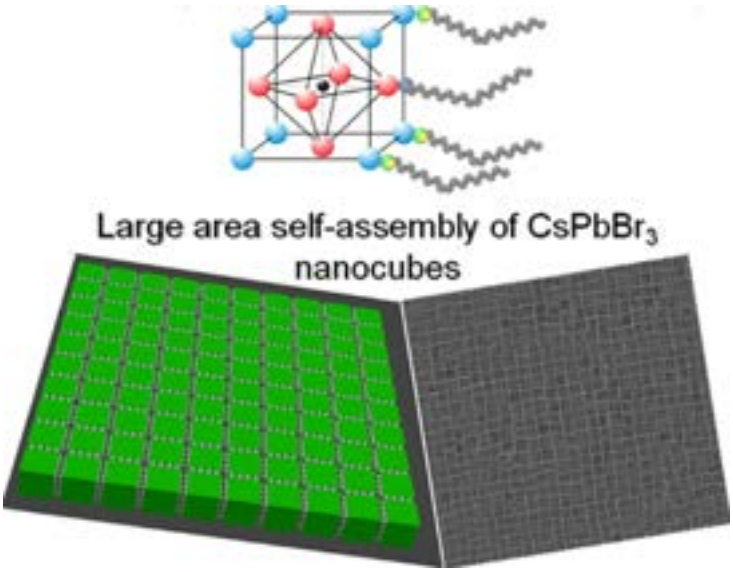

Figure 10: *Assembled nanocubes. Figure obtained from Patra et al.*[32]

After self-assembly of the perovskite nanocubes, MAPI could then be deposited on the nanocube monolayer. The nanocubes should act as a seed-layer for the deposited MAPI and all the different nucleation sites should follow the same orientation of the assembled nanocubes. A schematic view of this process can be seen in figure 11. In the next section, the method of experiment to achieve this is explained.

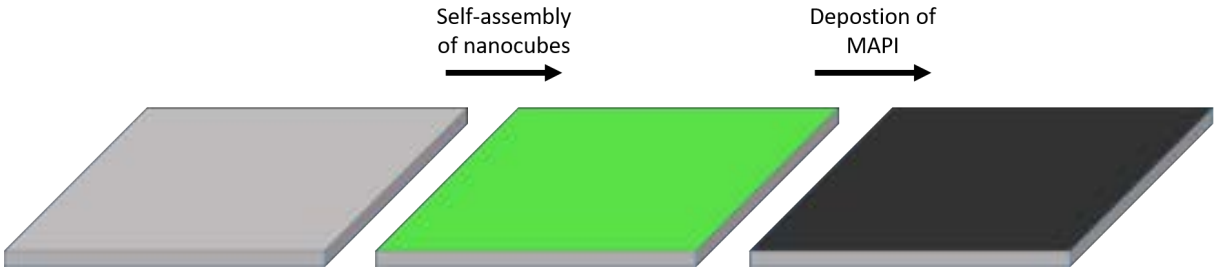

Figure 11: *Schematic view of the steps to deposit MAPI on top of a perovskite nanocube seed-layer.*

3 Methods

In this chapter, the method of experiment is explained. First is illustrated how a solution of $CsPbBr_3$ nanocubes in toluene is made. Second, the way to clean the silicon substrate is shown, followed by the technique used for self-assembly of said nanocubes. Finally will be explained what method is used to grow a layer of MAPI on the nanocubes and which parameters were set as a basis to compare the effect of adjusting specific parameters. The method of experiment will be followed by an explanation of how the properties of the prepared samples are characterized.

3.1 Sample Fabrication

3.1.1 Materials

Caesium carbonate (Cs_2CO_3 , >99.99%), lead bromide ($PbBr_2$ >99,99%), oleylamine (OLA >98%), oleic acid (OA, >90%), toluene (>99.99%), ammonium thiocyanate (NH_4SCN, 97.5%), methyl acetate (>99.5%) and lead iodide (PbI_2, >99.999%) were purchased from Sigma-Aldrich and 1-octadecene (ODE, 90%) and methylammoniumiodide (CH_3NH_3I , >99.0%) were purchased from TCI. All chemicals were used without further purification. All samples were prepared on Si <100> substrates with a size of either 6x6 or 12x12 mm.

3.1.2 Nanocube synthesis

The $CsPbBr_3$ nanocubes are fabricated via the hot-injection method. First, a 100 mL three-necked flask is filled with 0.814 gr of Cs_2CO_3, together with 2.5 mL OA and 40 mL ODE. Then, the flask is connected to the Schlenk line where the flask is purged with N_2 3 times to remove oxygen and then heated to 120 °C under vacuum to get rid of possible contamination by water. Then the solution is heated to 150 °C under N_2 for 2 hours so all Cs_2CO_3 reacts with OA. After 2 hours the temperature of the solution is set to 100 °C. In the meantime another 100 mL three-necked flask is filled with 0.69 gr of $PbBr_2$, together with 5 mL OA, 5 ml OLA and 30 mL ODE. Then, the flask is connected to the Schlenk line where the flask is also purged with N_2 3 times and dried at 120 °C under vacuum. After this the temperature is increased to 160 °C under N_2.

When both flasks have reached their right temperature, the hot-injection is started. While both flasks are still in a N_2 controlled environment, 4 ml of the Cs_2CO_3 solution is extracted with a syringe and quickly injected into the flask with $PbBr_2$ solution, as seen in figure 12. Immediately, the colour of the mixture will change from colourless to green-brown. The three-necked flask is then quickly removed from the heating source and put into an ice bath and cooled to roughly 16 °C. The colour of the solution has now changed to bright yellow-green and will illuminate when a 405 nm torch shines upon it. This is an indication that the $CsPbBr_3$ nanocubes have been formed. The solution is set aside till it reaches room temperature and then collected in vials.

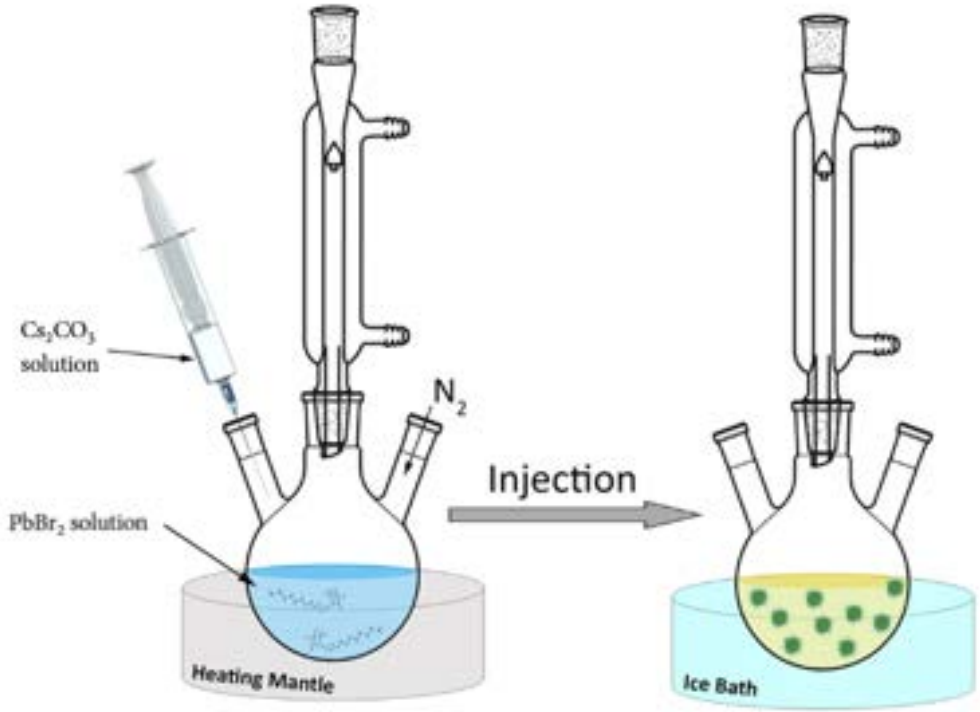

Figure 12: *Step in the process of the hot injection method where 4 ml of Cs_2CO_3 solution is injected in the PbI_2 solution, while heated to 160 °C and kept in a N_2 environment. Figure obtained from Shamsi et al.*[34]

To purify the nanocube solution the centrifuge is used. 6 Microtubes are filled with the nanocube solution and are centrifuged on 4310 RCF for 20 minutes. The supernatant is discarded and the microtube is carefully dried with a tissue while keeping the precipitate. The microtubes with the precipitate are centrifuged again on 4310 RCF for 20 minutes. Again the microtubes are dried with a tissue. Then, 1.5 mL of toluene is added to each microtube. The tubes are placed on a mini vortex to mix the content. Now the tubes are centrifuged again on 270 RCF for 10 minutes. The supernatant is collected in vials and diluted with toluene in a 2:1 ratio.

For the ligand exchange, 6 microtubes are all filled with 0.5 mL of the previously obtained solution and 1 mL of methyl acetate. The tubes are centrifuged on 4310 RCF for 20 minutes.

The supernatant is discarded and 0.5 mL toluene is added to each tube. The tubes are placed on a vortex and then centrifuged on 6740 RCF for 5 minutes. Now, 0.4 mL of the supernatant of each tube is collected in a vial. To add new ligands, 2 mL of the previously collected solution is transferred to the glovebox, where 50 mg of ammonium thiocyanate (NH_4SCN) is added to the solution. The mixture is then stirred for 30 minutes at 500 rpm. The solution is then distributed over 2 microtubes and centrifuged on 270 RCF for 5 min. The supernatant is collected and centrifuged again on 6740 RCF for 5 minutes. Repeat this step 2 extra times and collect the supernatant in a vial. The nanocube solution is now ready for self-assembly.

3.1.3 Substrate Preparation

To clean the silicon substrates prior to the self-assembly, the substrates are placed in a beaker with acetone and sonicated for 10 minutes. Right after this the samples are transferred to a beaker with 2-propanol and sonicated again for 10 minutes. These two cleaning steps are done in the cleanroom to avoid pollution. The samples are taken out of the beaker and are dried one by one by a N_2-gun. The samples are placed in a closed sample box and stored overnight so surface activation is over and will not affect the wetting of the substrate when the nanocube solution is dropped onto them.

3.1.4 Self-assembly

For the self-assembly of the $CsPbBr_3$ nanocubes, the clean substrates are placed in a toluene gas chamber. This chamber is simply made by placing a container upside down over the substrates and a smaller beaker filled with toluene, as seen in figure 13. For 6x6 mm substrates 6.25 μL and for 12x12 mm substrates 25 μL is dropcasted onto the substrates through a hole in the top beaker. The hole is closed by a plug immediately after. Overnight the solution on the substrates will slowly evaporate so enough time is available for the nanocubes to assemble themselves into an energetic favourable closed-packed order. The substrates with assembled nanocubes are finished the next day.

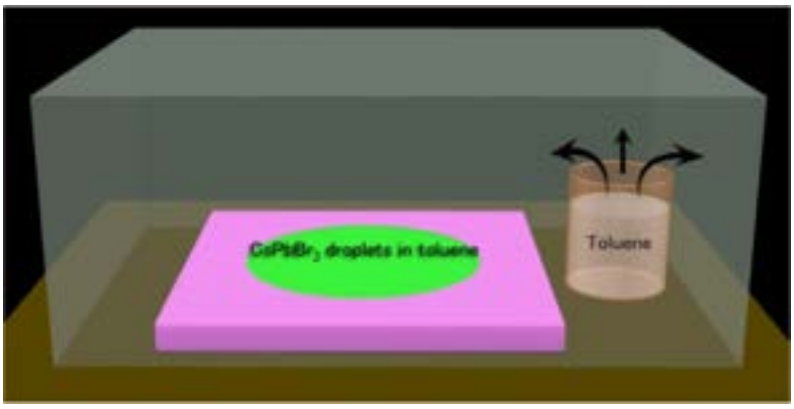

Figure 13: *Schematic view of toluene gaschamber.*

3.1.5 Chemical vapour deposition

To deposit the MAPI onto the substrate covered with the assembled nanocubes a one-step chemical vapour technique is used. Two 7 cm ceramic boats with precursors are loaded into a 75 cm quartz tube with a 22 mm diameter. One boat is filled on the right side with 50 mg of PbI_2 and in the tube 23.5 cm between the left edge of the boat and the left edge of the tube. The second boat is filled on the left corner with 250 mg of MAI and placed in the tube so the left edge of the boat is 15 cm separated from the left entrance of the tube. Now, there is 13 cm distance between the powdered precursors.

When using two 12x12 mm Si substrates, three substrates with a nanocube layer are placed on a quartz 15x100 mm quartz substrate next to each other 2 mm from the left side with 2 mm spacing between each other. When using 6x6 mm Si substrates, 3 substrates with nanocubes are placed in rows on the same 15x100 mm quartz substrate. The substrates are placed 1 mm from the left edge with 1 mm spacing in between them. Three substrates without nanocubes are placed directly on the other row. A double-sided tape is used to keep the substrates in place. Note that multiple silicon substrates are placed in a row because the tube oven used shows poor reproducibility and the deposition site of MAPI could therefore shift up to 1 cm horizontally. The quartz substrate with the silicon substrates is then pushed into the tube on the right side till the exact middle of the silicon substrate row is exactly 22.7 separated from the right side of the tube. The tube is then transferred to the tube oven and placed so that the left edge of the MAI boat is 3 cm from the left outer edge of the oven and the right inner edge of the oven is exactly aligned with the exact centre of placed rows of silicon. Figure 14 shows a schematic view of the set-up.

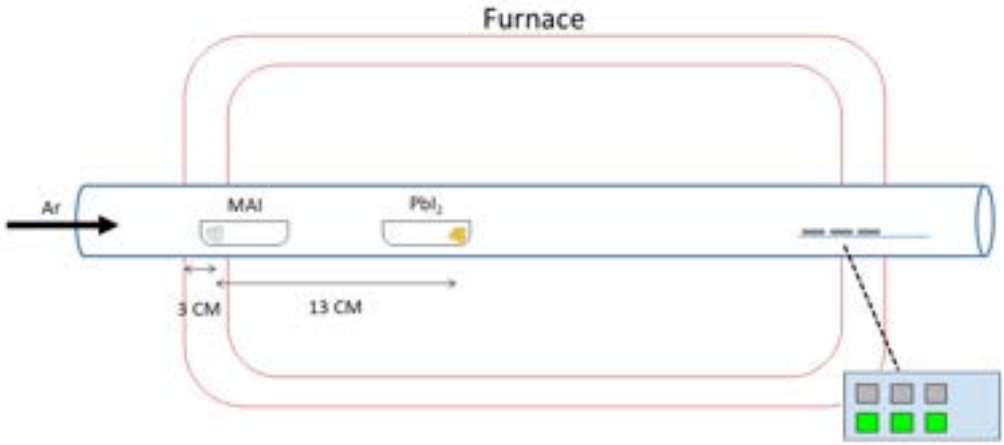

Figure 14: *Schematic view of CVD setup.*

The tube is connected to a vacuum pump and an argon gas flow. The tube is purged three times with argon to remove all oxygen in the tube. Then, a 100 sccm Argon gas flow is applied, while a constant vacuum is applied as well. The resulting pressure in the tube is set to 5,75 torr. The tube oven is then set to a ramping speed of 10 °C/min to 100 °C, followed by a ramping speed of 5 °C/min to 300 °C. The oven is set to dwell on 300 °C for 30 minutes. After 30 minutes the oven is opened and turned off. A yellow-orange deposition could be seen on the site of the substrates, which turns black by cooling down. Note that adjusting the dwelling time, ramping speed, pressure and maximum temperature will change the location of deposition and the morphology of the deposited MAPI layer. Finally, when the tube is cooled down to a safe temperature, the tube is disconnected from the vacuum and the argon airflow. The substrates are immediately taken out from the tube and placed in a glovebox to avoid degradation by humidity and oxygen.

3.1.6 Coating with PMMA

To avoid degradation by humidity and oxygen, the samples are coated with PMMA. This is done in the glovebox by spincoating. A PMMA-chlorobenzene solution with a concentration of 10 millimolar PMMA. The substrate is placed on a vacuum nozzle. 80 μm of the PMMA solution is dropped on the substrate and the substrate is set to 5000 RPM. After 30 seconds the rotations are stopped and the substrate is placed on a hotplate that is set to 100 °C and is set to dry for 15 minutes. After following these steps the created MAPI films on top of $CsPbBr_3$ nanocubes are investigated with characterisation techniques. In the following section, the equipment used for this characterization is explained.

3.2 Characterization

3.2.1 X-Ray Diffraction (XRD)

The X-ray diffraction patterns are obtained using a Bruker D2 phaser. The setup uses a Cu Kα tube to generate X-rays. The X-rays are created by the decay of electrons in copper atoms from the 2p shell to the 1s shell. In the 2p shell, two energy levels are occupied, namely the L_I and L_{II}. Because of these different energy levels, the X-rays could have either a wavelength of $\lambda = 1.5406\text{Å}$ or a wavelength of $\lambda = 1.5444\text{Å}$. The X-rays are sent onto the sample under a variable angle θ. The beams are diffracted by the crystal lattice. The diffracted beams then interfere according to Bragg´s law. Bragg´s law is written as:

$$n\lambda = 2d\sin\theta$$

Here, n is an integer which gives the peak order, lambda is the wavelength of the incoming beam, d is the in-plane distance between the atoms in the crystal and θ is the angle of incident. The reflected and interfered beams are collected at the opposite side of the incident X-ray beam at the same angle θ. A schematic overview is shown in figure 15. Following the equation, specific peaks will be shown at different angles depending on the interplanar distance of the lattice. The peaks are compared to peaks found in corresponding literature to see if the material is synthesized successfully and if the out-of-plane crystal orientation is equal over the whole sample.

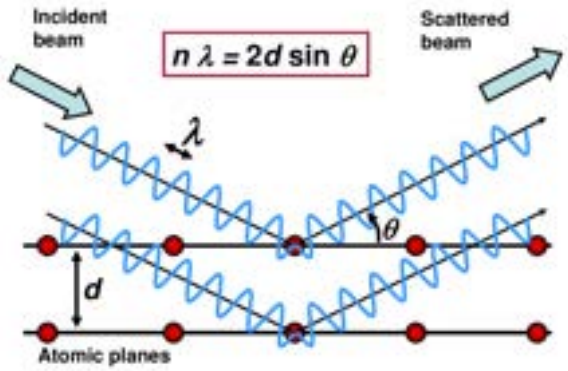

Figure 15: *Schematic view of reflected X-ray beams by a crystal lattice. Figure obtained from Nasir et al.*[35]

3.2.2 Scanning Electron Microscopy (SEM)

In this research, it is needed to investigate the produced samples beyond the diffraction limit. This can not be done by an optical microscope because this scale is smaller than the wavelength of observable light. So instead of photons, electrons are detected (which could have a much smaller wavelength). To image the produced samples a scanning electron microscope (SEM) Verios 460 from Thermo Fischer Scientific is used. A sample is placed onto the substrate and the chamber is pumped into a vacuum. An electron beam is sent and scattered upon the sample. The scattered electrons are driven into a detector and an image is created.

3.2.3 Energy-dispersive X-ray Spectroscopy (EDS)

To investigate which elements a material consists an EDX detector made by Oxford Instruments is used. The measurements are done in the Verios 460. The electron beam current is set at 100 pA at 10 kV. Electrons are fired at the substrate, which ionizes the atoms in the substrate because electrons from the inner shell are being removed by the incident electron. The gap left in the inner electron shell is filled by electrons from the outer shell by emitting a photon of corresponding energy in the X-ray regime. The intensity of different X-ray energies. Because specific X-ray energies are unique for different atoms, the measured X-rays and their intensity is used to compute the weight percentage of each atom. Measurements with EDS were done with the help of Hong Yu Sun.

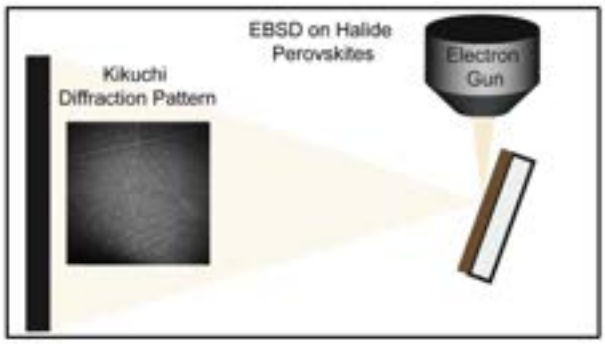

Figure 16: *Schematic view of EBSD setup. Figure obtained from Jariwala et al.*[18]

3.2.4 Electron Backscatter Diffraction (EBSD)

To measure the crystal orientation of the created thin film, a state-of-the-art solid-state EBSD detector is used. The measurements are done in the Verios 460. The beam current is set at 100 pA at 10 kV accelerating voltage with a pixel integration time of 90 ms. Kikuchi diffraction patterns are generated by measuring the backscattered electrons from the sample. The electrons hit the sample at 70° with respect to the normal of the sample surface, then they are diffracted by the crystal structure and then measured by the detector. The set-up is schematically shown in figure 16. Measurements with EBSD were done with the help of Hong Yu Sun.

3.2.5 Photoluminescence (PL)

The photoluminescence of the perovskite is measured with the WiTec. The perovskite sample is excited by a continuous 405 nm laser. By shining a laser onto the sample, carriers are created and recombined again. By radiative recombination photons, of the wavelength corresponding to the bandgap are emitted. A spectrometer obtains a signal from the emitted photons and shows the photoluminescence of the sample.

3.2.6 Time Resolved Single Photon Counting (TCSPC)

To measure the carrier lifetime of the perovskite samples, a home-build set-up was used. The set-up is equipped with a laser serving as an excitation source of 485 nm. The laser was set to pulse with a frequency of 10 MHz. With every pulse, the sample is excited and one emitted photon is detected. Then, a histogram is made where each time difference, from excitation to detection, is counted. The resulting histogram can be used to calculate the carrier lifetime of the sample. The measurements were done with the help of Sarah Gillespie.

4 Results and Discussion

In this section, the results of the measurements with the previously mentioned techniques are shown and discussed using the theory from section 2. This section starts by showing SEM pictures of the self-assembled nanocube layer, followed by results that show the consequence of heat and other parameters of the CVD on the assembled nanocube layer. Then samples of thin-film MAPI overgrown on the nanocubes using different parameters, such as dwelling time and vacuum are shown to demonstrate the influence of said parameters. Finally, the achieved champion thin-film of MAPI is demonstrated, accompanied by the measured properties of this film.

4.1 Assembled nanocube layer

After synthesis of the toluene-nanocube solution and self-assembly, the substrates were investigated by XRD. Figure 18 shows the XRD-pattern of the film. By comparison with literature,[32] it is clear that the fabricated layer is indeed made of $CsPbBr_3$. The noise seen in the graph is due to the fact that the cubes are only 10 nm thick.

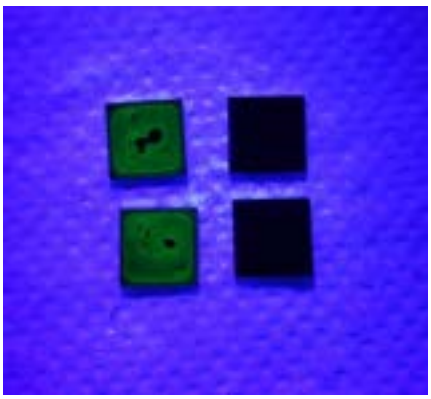

Figure 17: *Silicon substrates with nanocube layer under a 405 nm torch. The samples on the left have not been in the CVD oven, the samples on the right have been in the CVD oven*

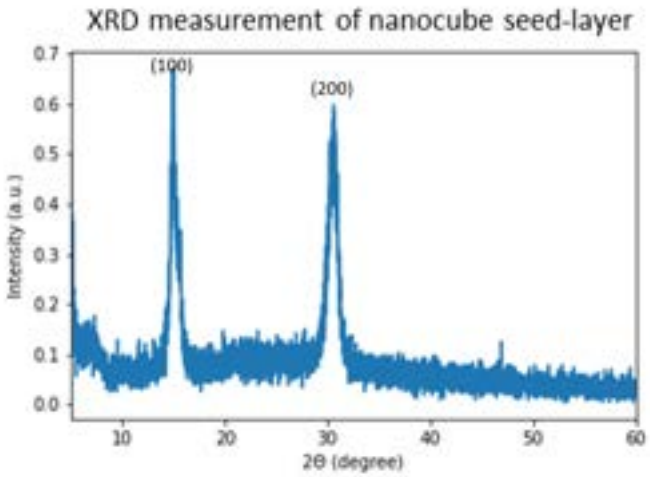

Figure 18: *XRD measurement of assembled $CsPbBr_3$ nanocube monolayer.*

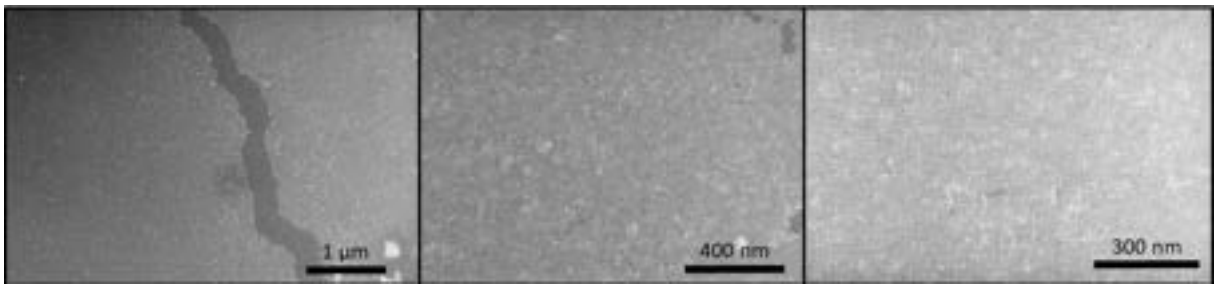

Figure 19: *SEM pictures of assembled $CsPbBr_3$ nanocube monolayer.*

Figure 17 shows substrates illuminated by a 405 nm torch. The substrates emit a bright greenish colour. Images made by SEM (figure 19) show that the nanocubes are self-assembled to a closed-packed layer of nanocubes. The cubes have a width of 10 nm on average, which is in agreement with the replicated recipe of Patra et al.[32] Overall, the layer seems to be a monolayer on the majority of the sample.

To see how the environment of the process of CVD acts on the assembled layer of nanocubes, test runs were done without adding precursors to the CVD process. Again the resulting samples were imaged by SEM. Figure 20 shows these images. It is clear to see that the environment of the CVD process affects the morphology of the nanocubes.

When shining a 405 nm torch on the substrate, no luminescence is to be seen, as seen in figure 17. This indicates that the material is degraded. In the pictures made by SEM no distinct cubes are to be seen, which could imply that the ligands capping the cubes are evaporated and therefore the cubes have merged. Evaporation of the ligands could lead to a different interaction between the silicon surface and the $CsPbBr_3$ layer which results in dewetting of the $CsPbBr_3$ on the substrate. It seems that the cubes find merging together to islands is more favourable than staying spread out on the surface. While the merging of the $CsPbBr_3$ nanocubes is detrimental for the nanocubes to act as a uniform seed-layer, still it is useful to investigate if the deposition of MAPI on top of the $CsPbBr_3$ layer has clear differences with a deposited layer of MAPI on bare silicon. That is to say, there is a possibility that during the deposition process, the overgrowth of MAPI takes place before or while the cubes are merging into bulk $CsPbBr_3$, weakening the process of merging itself. In the next section, this experiment is analysed.

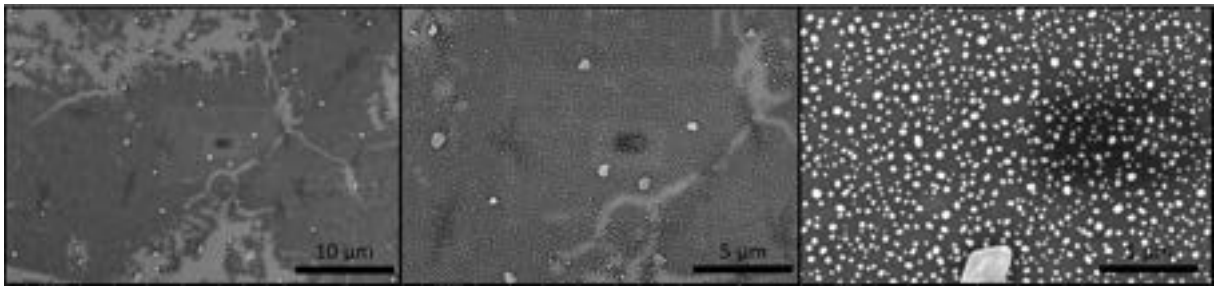

Figure 20: *SEM pictures of $CsPbBr_3$ layer after a full CVD run.*

4.2 Effects of nanocubes on the depostion of MAPI

To investigate the difference the layer of nanocubes makes on the deposition of MAPI by CVD, the setup as discussed in section 3.1.5 was used. Because both the samples, with and without nanocubes, are prepared in the same experimental run, it's acceptable to compare the different samples with each other. Figure 21 shows the XRD results of the deposited films on bare silicon and on silicon covered by a self-assembled layer of $CsPbBr_3$ nanocubes. Compared with literature, this shows the deposited film is indeed MAPI in both cases.[36] The low counts and noise seen in the measurement of the deposited MAPI on the bare silicon sample compared to the other sample could be a result of less deposited material.

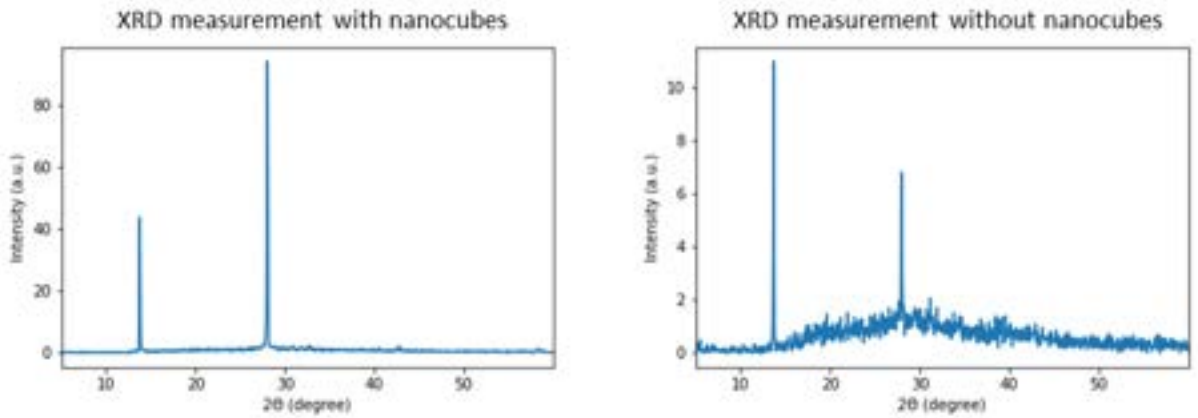

Figure 21: *XRD meassurements of substrates with deposited MAPI with and without a nanocube seed-layer.*

Figure 22 show SEM images of both substrates. It is evident that utilising the nanocubes as seed-layer has a positive effect on the density of nucleated MAPI onto the substrate. Excluding the nanocube layer, results in the nucleation of poorly oriented small crystals. Including the seed-layer, however, results in the crystallisation of bigger crystals. The difference in density of deposited material is in agreement with the previous statement done as a consequence of the XRD measurements. Furthermore, the crystals seem to be oriented in the same direction. The oriented organization of the crystal islands of MAPI could indicate that the nanocube seed-layer has acted as a template for well-oriented crystal growth.

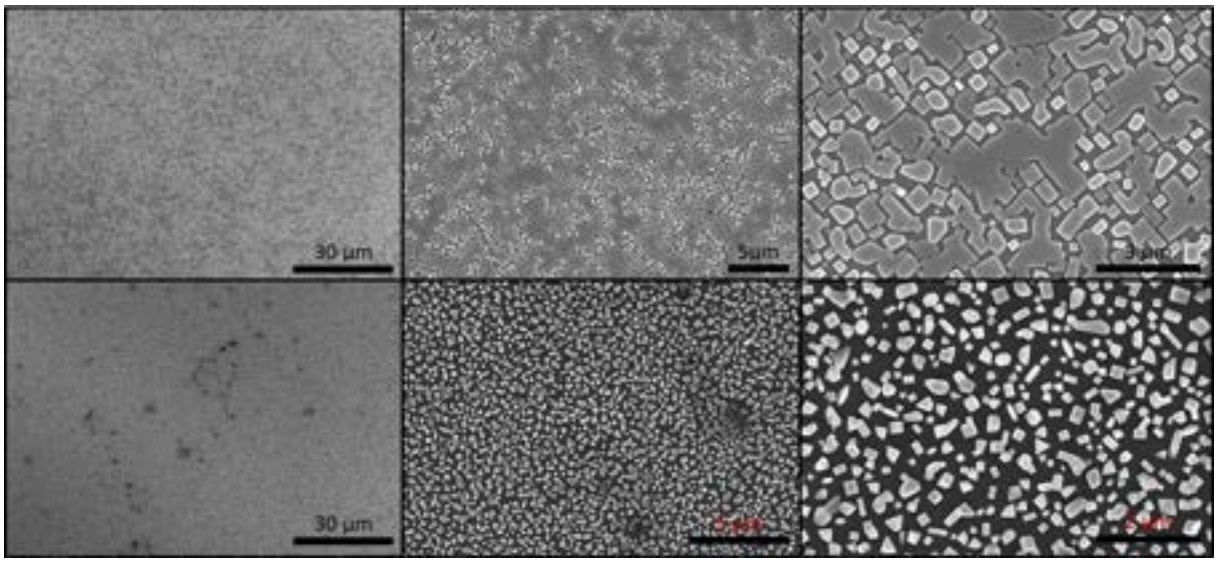

Figure 22: *SEM pictures deposited MAPI. The top row shows MAPI deposited on the nanocube layer. The bottom row shows deposition without nanocube layer.*

It is evident that utilizing a nanocube seed layer has positive effects on nucleation and orientation, but not all islands are oriented in the same direction. This could be a consequence of different processes. As seen in section 2.5 the cubes could have merged and formed their own islands. Another reason for this non-uniformity in orientation is that the assembled seed layer is not perfectly assembled in the same direction, i.e. curves and bends are present in the layer.

To be applicable for devices the perovskite thin film needs to be a uniform fully covered film. In the next section, results are shown of different experiments where parameters are changed in an attempt to achieve uniform film. The results are additionally analysed to understand the deposition mechanism.

4.3 Road to a perfect film

In previous sections, claims are made that adding a nanocube layer positively affects the epitaxial growth of thin film MAPI. Still, with the used parameters, the fabrication of full-packed MAPI film has not been achieved. In this section, the intermediate results of the process to achieve a uniform film are shown and discussed. The effect of adjusting parameters like deposition time and pressure are shown and analysed. The XRD measurements to prove each sample contains a layer of MAPI in the cubic phase can be found in section S.1.

4.3.1 Increasing deposition time

The images in section 4.2 show that a full uniform film has not been achieved. Adjusting the parameters could stimulate creating a fully covered film. Previous research shows that increasing the dwelling time of the process will increase the amount of deposited precursor and therefore cover the full substrate.[29] Taking the different epitaxial growing modes from section 2.4 into account, increasing the deposition time seems to be a logical first step to achieve a fully covered film. Figure 23 show SEM figures of samples where the dwelling time was set to 60 and 90 minutes instead of 30 minutes.

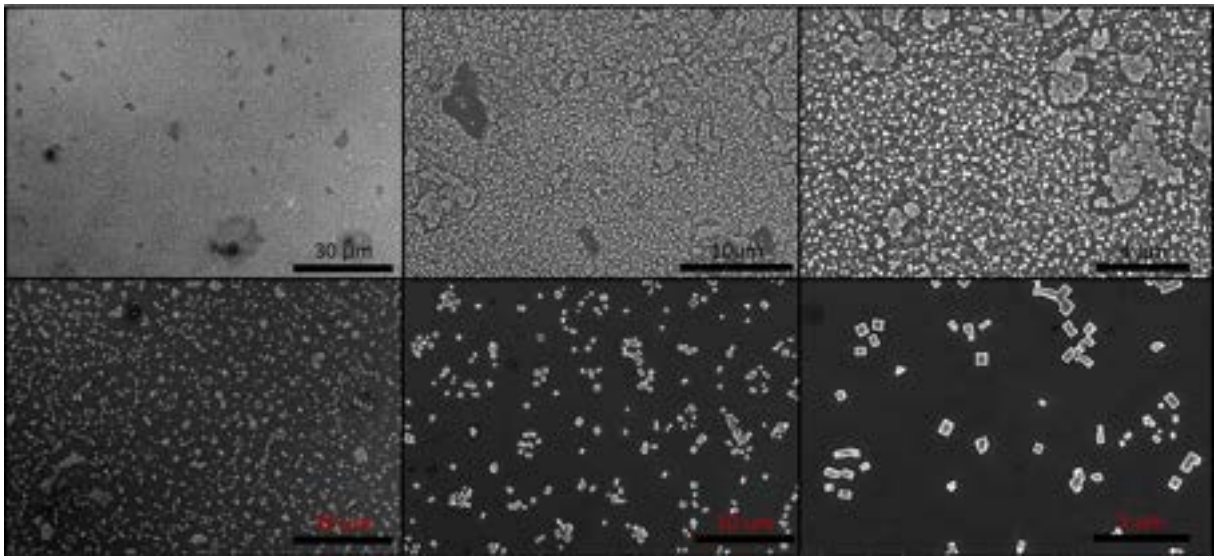

Figure 23: *SEM pictures of deposited MAPI on top of the nanocube seedlayer. The top row show the results for a deposition of 60 minutes and the bottom row for a deposition of 90 minutes.*

Although it was expected that the film would get denser, it is clear to see that the formed islands shrink in size of their surface and even seem to decrease in number. One simple explanation for this result is the reduction of the amount of precursor during the process. At the deposition site, the deposited MAPI is in a phase equilibrium of crystallisation and evaporation. Because the evaporation rate of the precursors decreases due to reducing in amount, the evaporation rate at the deposition site could get higher than the deposition rate. The high amount of precursor left after the experiment and the thickening layer of deposited material on the inside of the tube suggest, however, that this is not the case.

4.3.2 Decreasing pressure

A different approach to increase the amount of deposited material on the film to make the film denser is to increase the evaporation rate of the precursors. A way to do this, without the need to adjust other parameters, like the position of precursor and substrate is to decrease the pressure in the system. Figure 24 show the results of experiments where the pressure has been decreased.

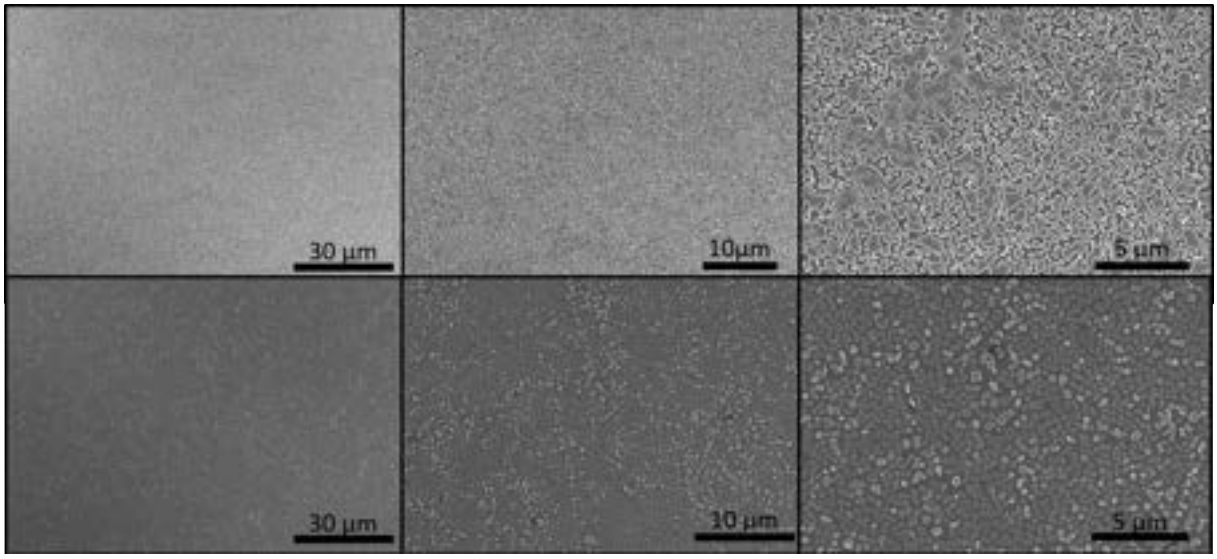

Figure 24: *SEM pictures of deposited MAPI on top of the nanocube seedlayer. The top row show the results where a pressure of 3.1 torr is maintained and the bottom row shows the results for a presure of 2.0 torr.*

The results show that the deposited film doesn't seem to get denser compared to the previously used pressure of 3.6 torr. While the resulting SEM pictures show the island formed are evenly distributed, no full pack film seems to be fabricated. In the next section, the obtained results are analysed so new steps can be taken to improve the fabricated film.

4.3.3 Analysing results

A possible reason that is investigated is the possibility of Stranski-Krastanov growth, mentioned in 2.4. A full uniform layer of MAPI could have already been formed and because of the increasing strain energy, the growth continues in islands that get higher and smaller to minimize surface energy. The first formed bottom layer could be hard to image with SEM because of contrast differences, making the bottom layer appear like a smooth silicon surface. Regarding figure 8 this suggestion can be falsified by EDS measurement on the sample. Figure 25 shows that the area between the islands does not contain traces of MAPI precursors which suggests that no Stranski-Krastanov growing mode is followed during deposition. Furthermore, the EDS measurement also shows no $CsPbBr_3$ is present in between the islands whilst being present in the islands.

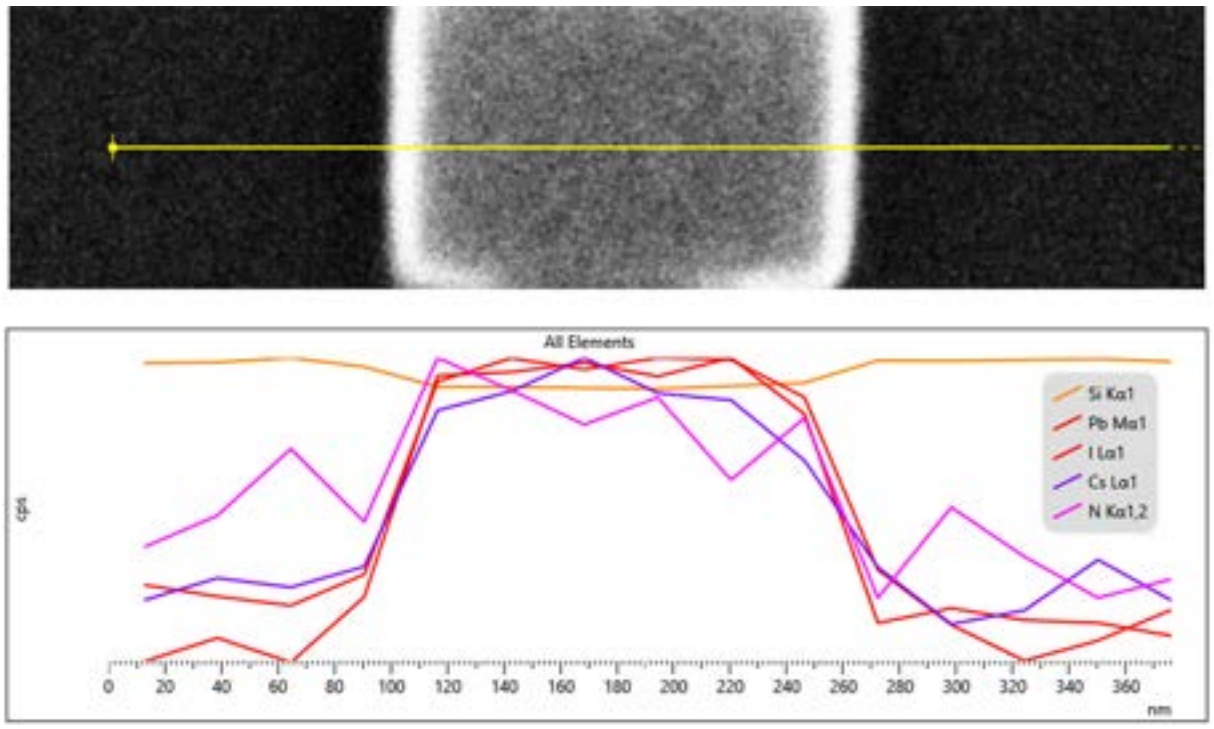

Figure 25: *EDS measurement on a crystal formed and the area around it. The sample that which had a deposition time of 60 minutes was used.*

This observation gives rise to the idea that the $CsPbBr_3$ still tends to merge underneath the deposited MAPI to minimize the surface energy. The deposited MAPI follows the movement of the $CsPbBr_3$ and therefore reassemble themselves in cubic islands.

4.3.4 Decreasing deposition time

Due to the kinetic mobility of the $CsPbBr_3$ layer, increasing the deposition time or decreasing the pressure does not improve the uniformity of the film. It does raise the question if the $CsPbBr_3$ in the previous experiment with 30 minutes of deposition time (figure 22) a uniform film already was formed and the seed-layer has already started merging or if the balance in deposition and re-evaporation has already been tilted within 30 minutes. Extra experiments were done with a short deposition time. The images in figure 26 show the morphology of the fabricated films. The first experiment, where a 5-minute deposition time is applied, shows multiple small crystal structures, which appear to be somewhat oriented in the same direction. Applying a deposition time of 10 minutes results in the growth of the nucleated crystal structure until grains meet and form boundaries. From 15 minutes and longer it seems that connected grains merge by annealing, so new islands are being formed. This could be the result of the movement of the $CsPbBr_3$ underneath. Increasing the deposition time further results in a better-oriented structure with bigger crystal islands on average.

Previous results show that changing parameters that affect the environment of the whole system, also affect the morphology of the $CsPbBr_3$ seed layer. The only parameter that could be changed that is not invasive for the seed-layer and will not change the deposition site is changing the amount of precursor in the boats. Increasing the amount of precursor will increase the evaporation rate and therefore, most likely, increase the uniformity of the fabricated MAPI film. The next section will show the results of these new adjusted parameters.

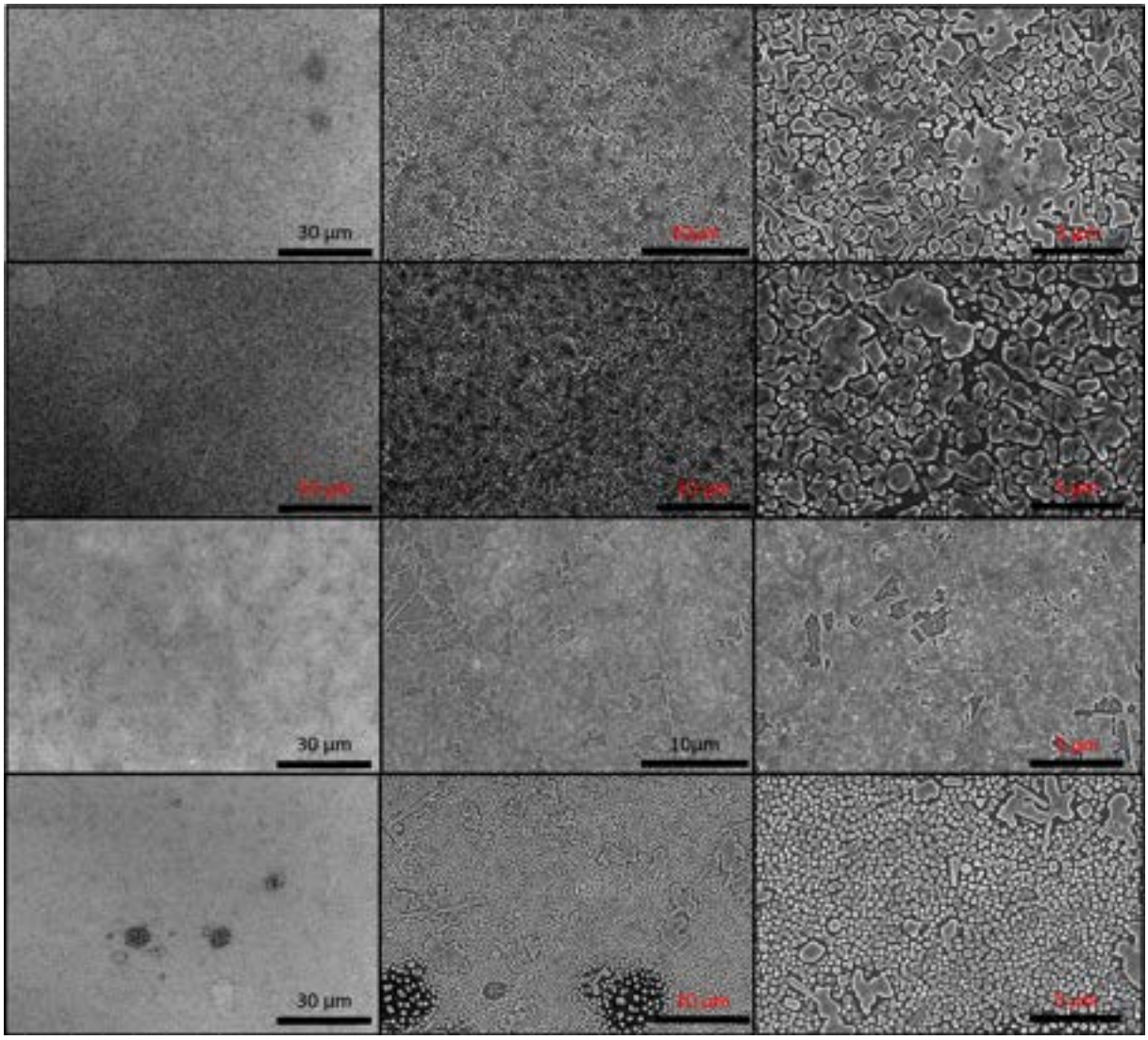

Figure 26: *SEM pictures of deposited MAPI. The first row shows pictures of a sample where a deposition time of 25 minutes is used. For the second row, a deposition time of 15 minutes was used, for the third row 10 minutes and for the bottom row 5 minutes.*

4.4 Characterisation of champion film

Figure 27 shows the morphology of the fabricated film by using the basis parameters stated in section 3.1.5, but doubling the amount precursor to 100 mg PbI_2 and 500 mg MAI. It is clear to see that the film is not fully packed, but improvements were made compared to previous results. While this research didn't achieve the goal of creating a fully covered MAPI thin-film by the CVD growing method, still it's of great importance to test some of the properties of the created film that is closest to the goal. This section starts with an analysis of images made by SEM, followed by the results of EBSD measurements. Finally, the luminescence and carrier lifetime of the champion film is investigated and compared to literature to investigate if the used method could compete with traditional methods for device applications.

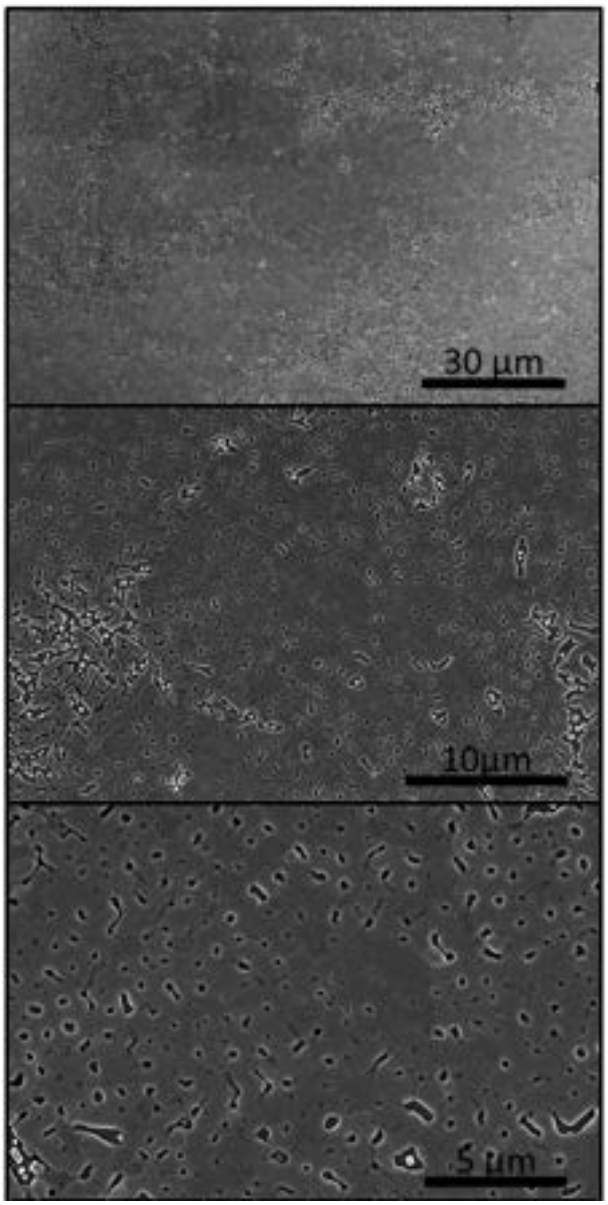

Figure 27: *SEM pictures of the most uniform and oriented film fabricated by the CVD method stated in section 3.1.5, but with doubling the amount of precursor.*

4.4.1 Crystal orientation

In several regions, the deposition almost resulted in a completely covered film. The pinholes and discontinuities in the film appear to have a certain orientation, which could be the result of nucleation, followed by oriented growth on top of the assembled $CsPbBr_3$ layer underneath. XRD and EBSD measurements were done to check if the neighbouring crystals indeed share the same crystal orientation. Figure 28 shows the XRD measurement of the sample. It is clear that MAPI has been fabricated and that in the out-of-plane direction the crystal is uniformly oriented.

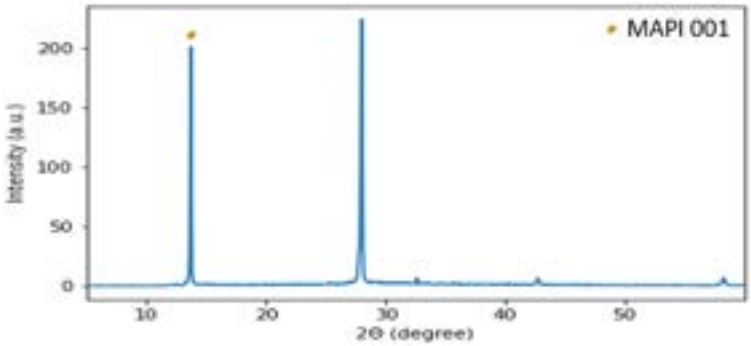

Figure 28: *XRD measurement of the fabricated MAPI film. The narrow peaks indicate a highly oriented film in the out-of-plane direction.*

Since XRD measurements only probe the out-of-plane (001) orientation, EBSD is used to prove the uniform orientation in the 001 direction and to investigate the in-plane (100) orientation. Figure 29 show the results of these measurements. Areas with the same orientation angle are depicted with the same colour. The images, however, also show noise, indicated by the grey areas. This does not necessarily mean that no orientation is present in these parts. The noise is possibly a result of declination in the film around the pinholes and gaps. At parts where the film is not horizontal flat, the diffracted electrons used for imaging could be refracted in various directions, causing noise. Nevertheless, it's clear to see, looking at the inverse pole figures for the (001) direction for both maps, that the crystal structures in both films are oriented in the same direction, which agrees with the XRD measurement.

The inverse pole figure for the (100) direction corresponding to figure 29a shows that different grains share almost the exact same orientation. The line scans, calculating the angle of misorientation, performed on the map (section S.2), show that the maximum angle misorientation of grains over the whole map is only about 5 degrees. The region shown in 29d and its corresponding inverse pole figure show a somewhat higher angle of misorientation between different grains. The maximum angle of misorientation between neighbouring grains is around 10 degrees. The angle of misorientation between the grains overall could be a consequence of misalignments in the orientation of assembled nanocubes. Comparing these

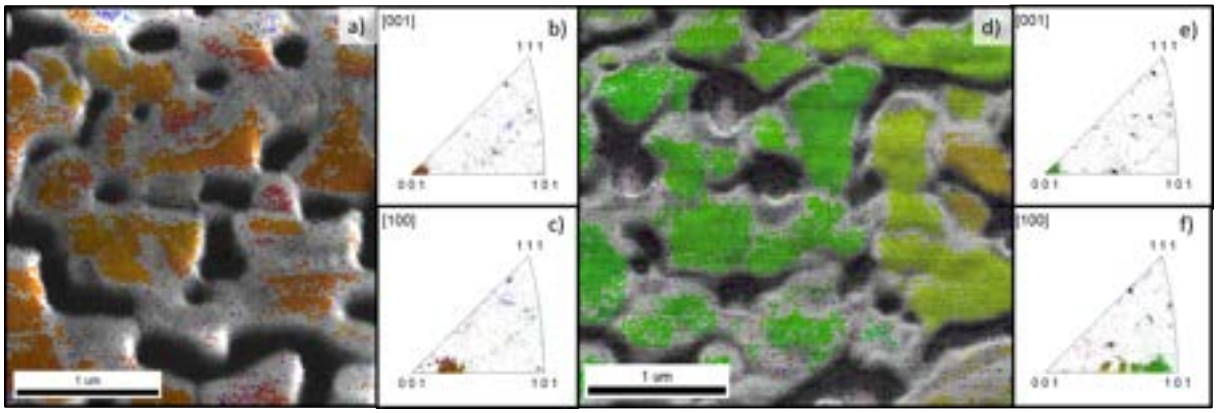

Figure 29: *a) & d) Images made by EBSD, colours depict the crystal orientation. The grey area indicates noisy signal and the black area indicates holes in the film. b) & c) show the 001 and 100 inverse pole figure, respectively, for figure a). e) & f) show the 001 and 100 inverse pole figure, respectively, for figure d).*

results with measurements done on a spincoated MAPI film without the use of a nanocube seed-layer, as seen in section 4 in figure 6, shows that the film which uses a nanocube seed-layer has an improved agreement in orientation of the crystal structure. Considering this, and the fact that the films shown in figures 29a and 29d did not grow from one nucleation site, but from multiple nucleation sites, namely the seed-layer, it's acceptable to state that agreement in orientation is due to the assembled perovskite nanocube seed-layer and template-assisted grow did occur. A possibility is that this agreement in orientation even arose from epitaxial overgrowth. To claim this, however, more evidence is needed.

4.4.2 Optoelectronic properties

Figure 30 shows the photoluminescence of the MAPI substrate. The peak wavelength is measured at 763.8 nm, which corresponds to 1.62 eV. Literature states that the bandgap of MAPI is around 1.58 eV, so the peak wavelength seems to be blue-shifted.[2137] Considering the fact that the bandgap of $CsPbBr_3$ is around 1.66 eV,[3839] this could be an indication that the $CsPbBr_3$ has mixed with the deposited MAPI instead of remaining underneath the deposited MAPI film. If this is the case, no epitaxial growth did occur. However, regarding the well-oriented morphology of the MAPI film, the seed layer did allow for template-assisted growth. The FWHM of the PL curve is measured to be 41.75 nm. This is rather narrow for a MAPI thin film. This could be contributed to the agreement in orientation of the formed crystals.

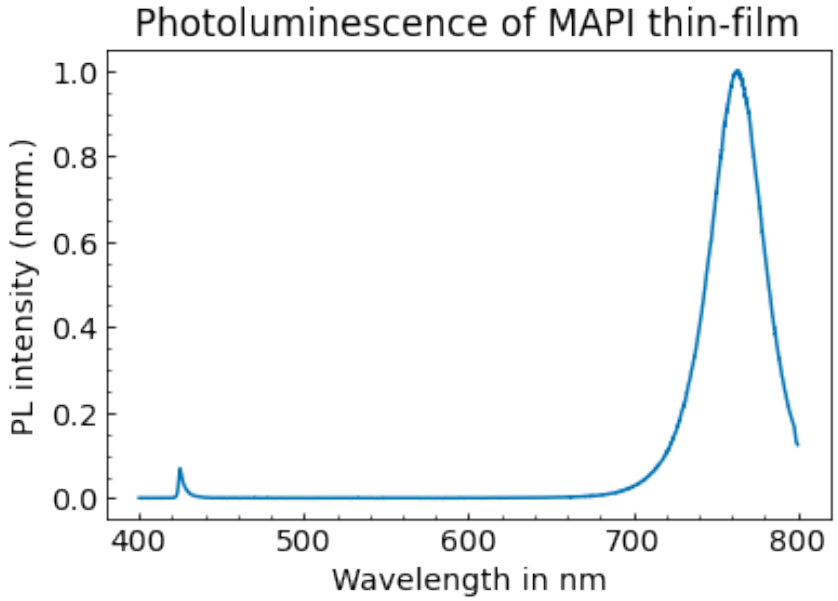

Figure 30: *Photoluminescence of the fabricated MAPI film. Created by shining a 405 nm laser on it. The small peak at around 425 nm is an artefact of the excitation source.*

The measured carrier lifetime is shown in figure 31. Data from this measurement show that $\tau_1 = 13ns \pm 0.2ns$ and $\tau_2 = 2ns \pm 0.1$. This is somewhat lower than the lifetimes measured in literature,[23] but it is a promising result considering the fact that the film is not complete. The measured properties show that, even though the fabricated film is not completely uniform, the photoluminescence and lifetime are comparable to traditional spincoat methods. In the next section, the results of the research are summarized and concluded. Finally, an outlook is given for future research and ideas are stated to achieve a fully covered perovskite thin-film.

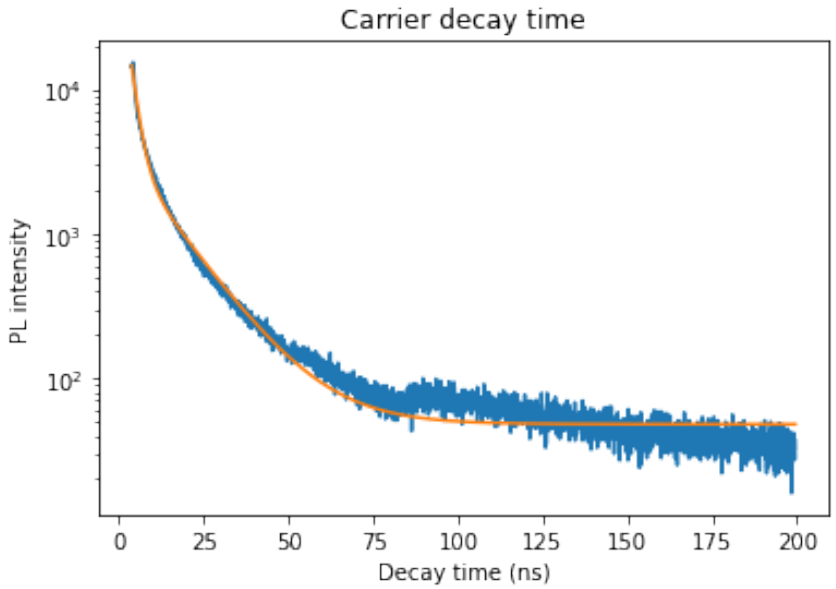

Figure 31: *Time-Correlated Single Photon Counting (TCSPC) data of the PL of a MAPI film. The orange line represents a fit to the data*

5 Conclusion and Outlook

In this last section, the research done is briefly summarised and concluded. This is followed by an outlook for future research on this topic. Ideas and suggestions are given to improve the fabricated film.

In summary, this research has investigated the possibility to utilize a seed layer of self-assembled perovskite nanocubes for well-oriented overgrowth of a different perovskite. Results have shown that applying such seed-layer affects the growth of the film by imposing a consistent orientation on the nucleated crystals. When using a nanocube seed-layer, nucleated crystals show an agreement in orientation, but when deposited on bare silicon the crystallites that originated at different nucleation sites are not well oriented.

This research suggests that well-oriented overgrowth of a perovskite thin-film is achieved by utilizing a nanocube seed-layer as a template. However, this research does not give satisfactory proof of epitaxial growth. In future research, the occurrence of epitaxial growth can be proven by investigating a crosscut of the sample with a transmission electron microscope (TEM). With this technique, the crystal structure of the material could be seen on atomic resolution.

Furthermore, this research suggests that ion exchange could have occurred, which means no $CsPbBr_3$ is present at the bottom of the film, but the perovskites have mixed completely, with a blue-shifted peak wavelength in PL as result.

The fabricated perovskite film as the end result did not fulfil the objective stated at the beginning of the project. The film that was finally achieved, showed to have pinholes and gaps. In future research, to fabricate a highly oriented perovskite uniform thin-film, the following steps can be taken.

First, a method could be used where the nanocubes seed-layer stays perfectly assembled and does not move during the deposition process. This research has shown that the use of CVD is invasive on the seed-layer by evaporating the ligands and dewetting the film. It is therefore recommended to make use of a deposition method which doesn't impose high temperatures on the substrate. A method that could be looked into is physical vapour deposition (PVD). With this technique, the substrate can be kept at a fixed low temperature so the cubes will experience less freedom to move. Because the substrate is not heated, the ligands will possibly not evaporate. The presence of ligands can have a negative effect on the template-assisted overgrowth of the perovskite. Therefore the substrate can be treated with flash annealing, before commencing PVD, so the organic ligands can evaporate and the nanocubes will merge into large mono-layered squares.

Another way to improve the film is to improve the assembled structure of the nanocube seed-layer. It is suggested to investigate different techniques to increase the orientation over bigger areas. A method for this could be self-assembly on a liquid-air interface to avoid the

coffee-ring-effect.

Because the process to achieve perfect uniform well-oriented film can be complicated, it is also possible to improve the quality by post-treatment, without improving the fabricated film itself. The gaps and pinholes can be filled with, for example, nanocubes to act as a passivation layer.

In conclusion, while this research did not prove the occurrence of epitaxial growth, this research did show that utilizing an assembled $CsPbBr_3$ nanocube seed-layer can be promising for the fabrication of a well-oriented perovskite thin-film by acting as a template for overgrowth.

Acknowledgements

For my research, I have been working at both AMOLF and the UvA. At both locations, I had a good time and I will look back at this last year with a positive feeling.

Having said that, I want to take a moment to thank some specific people who helped me during my research. First I want to thank Erik and Peter for being my supervisors and helping me get through this thesis. I enjoyed discussions during group meetings and valued both of your opinions greatly. Second, I want to thank Susan for being my daily supervisor and supporting me with her wisdom and kindness. I want to thank Hongyu for all the discussions we had about overgrowth on nanocubes, for the fun conversations and for the advice about doing a PhD after this. I want to thank Sarah for the good laughs and for explaining many different things. I want to thank Elaina for being a grand colleague, and for being really funny. I look forward to working with you during our PhD. Rohit, thanks for the advice about presenting and writing. Eitan, thanks for all your wise advice concerning almost everything. I want to thank Maryam for helping me set up this whole research and for showing me how everything is done. And, of course Marc, thanks for all the technical support. I want to thank the rest of the Nanoscale Solar Cell group for helping me with measurements and for the very kind, relaxed and 'gezellige' vibe. I also want to thank Marcel and Bauke from Peters group for discussing science, but mostly for the nice time, we had every Wednesday when I went to the UvA. I want to thank the whole group of course for thinking along with me about my project and giving advice on what to do next.

I want to show appreciation for Menke, Oscar and Kaj for joking around, discussing all kinds of stuff and for the frequent banter that helped us get through the day.

I want to thank my friends and family for supporting me this whole period. And to conclude, I want to thank my girlfriend Wies for supporting and enduring me during the writing of this thesis and for listening to all my scientific thoughts and trying to understand it all.

Supplementary Material

In this section figures are shown to support the claims and suggestions made in this thesis. XRD measuremens are shown to prove the fabrication MAPI-films. Maps made by EBSD, with correpsonding line-scans, are illustrated to show the angle of misorientation between formed grains.

S.1 XRD measurements of fabricated MAPI-films

Figures S1, S2 and S3 show the XRD-measurements on the deposited MAPI samples. Noise in the measurements could be attributed to a less oriented crystal film. The peaks shown in the XRD measurements at either side of the 14° peak for a 15 minutes deposition time are a result of PbI_2 present in the film.

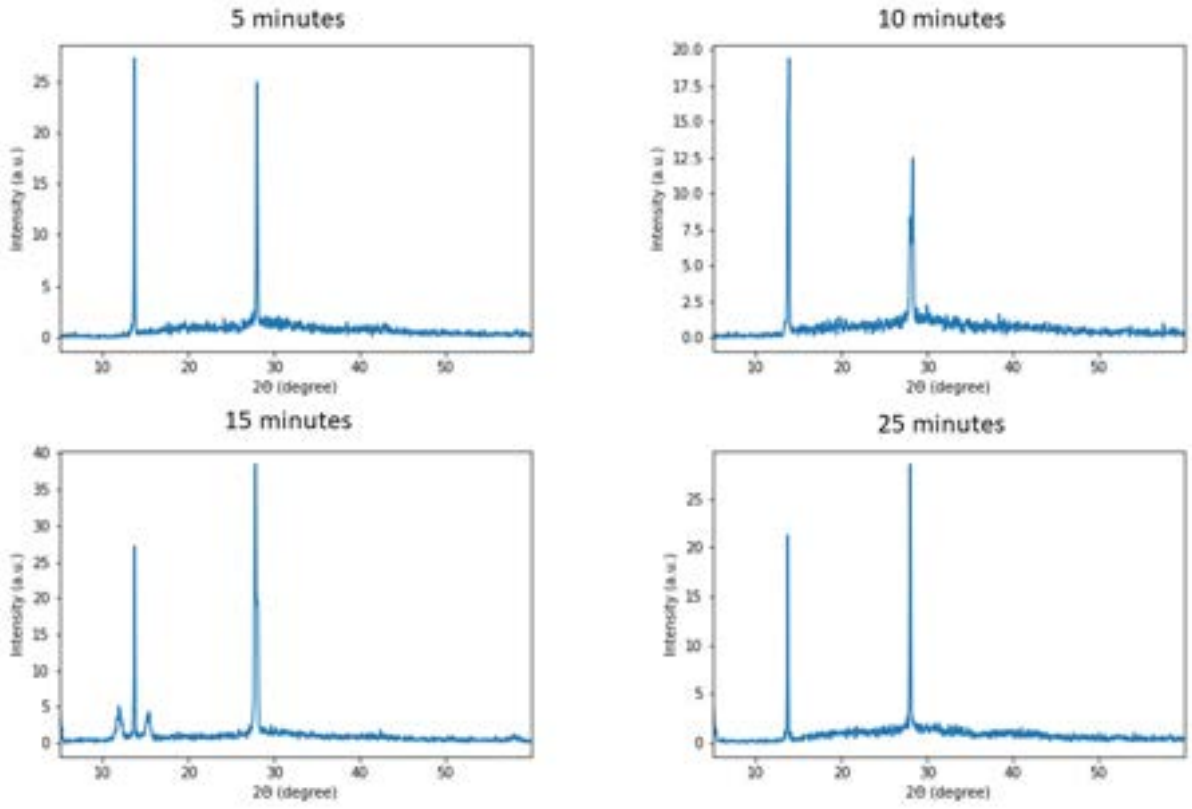

Figure S1: *XRD measurements of deposited MAPI. The deposition time is given.*

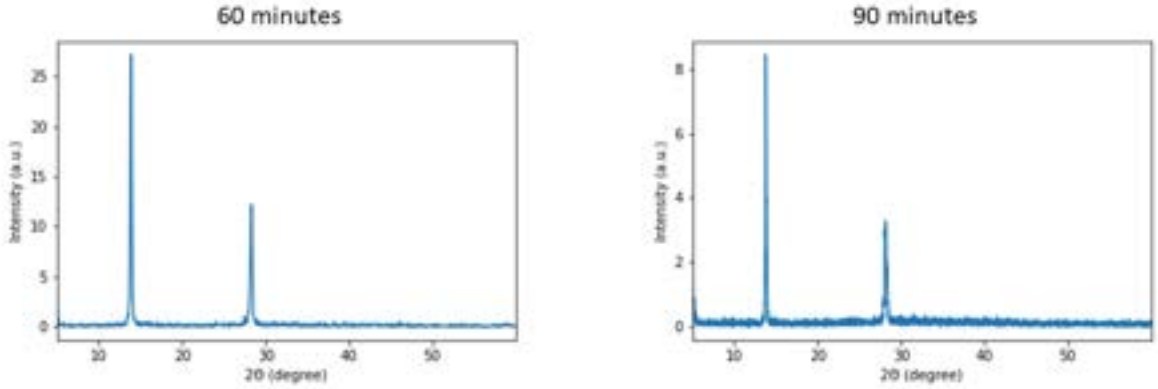

Figure S2: *XRD measurements of deposited MAPI. The deposition time is given*

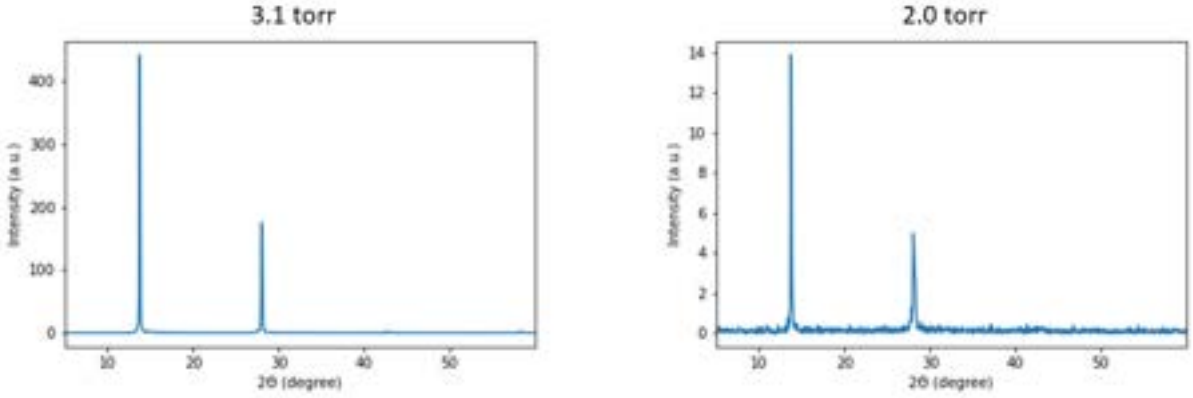

Figure S3: *XRD measurements of deposited MAPI. The pressure is given*

S.2 EBSD measurements of fabricated champiom MAPI-films

In this section the results of the measurements done by EBSD are shown. Line-scans are given to show the angle of misorentation between formed grains. The begin point of every arrow is taken as a basis for orientation and the a

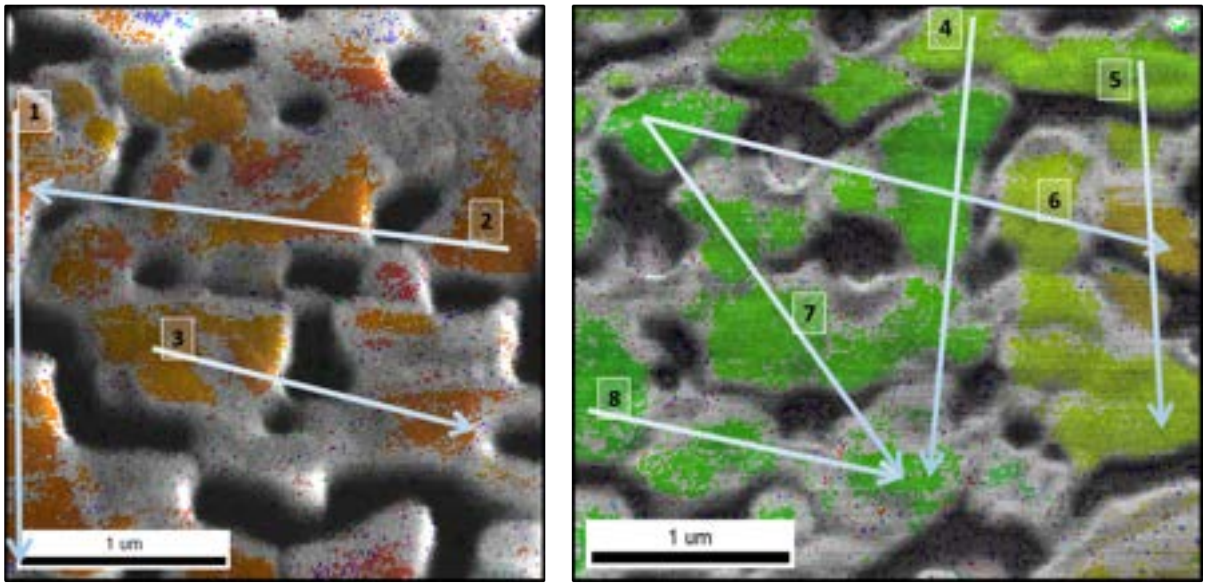

Figure S4: *Figure made by EBSD. The figure shows different crystallisations in the grains. The lines represent line scans done to investigate the misorientation between the grains crossed by the line and the grain at the start of the line at the blue region*

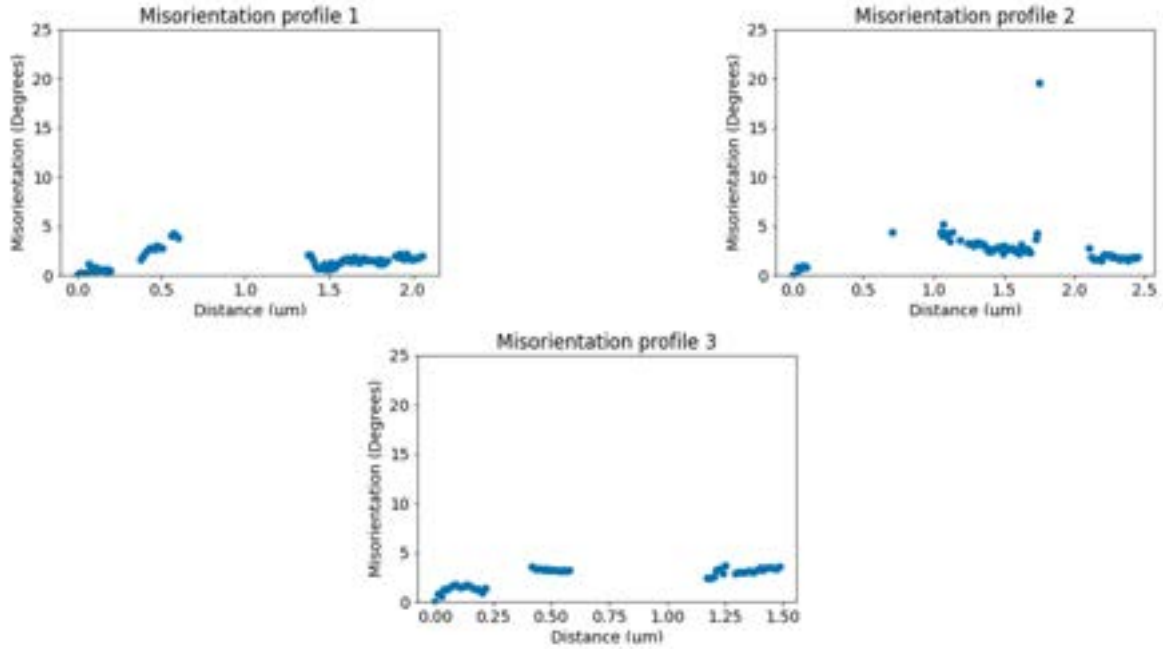

Figure S5: *Misorientation in degrees of line-scan 1 till 3. The noise coming from the gaps between the grains is masked from the plot*

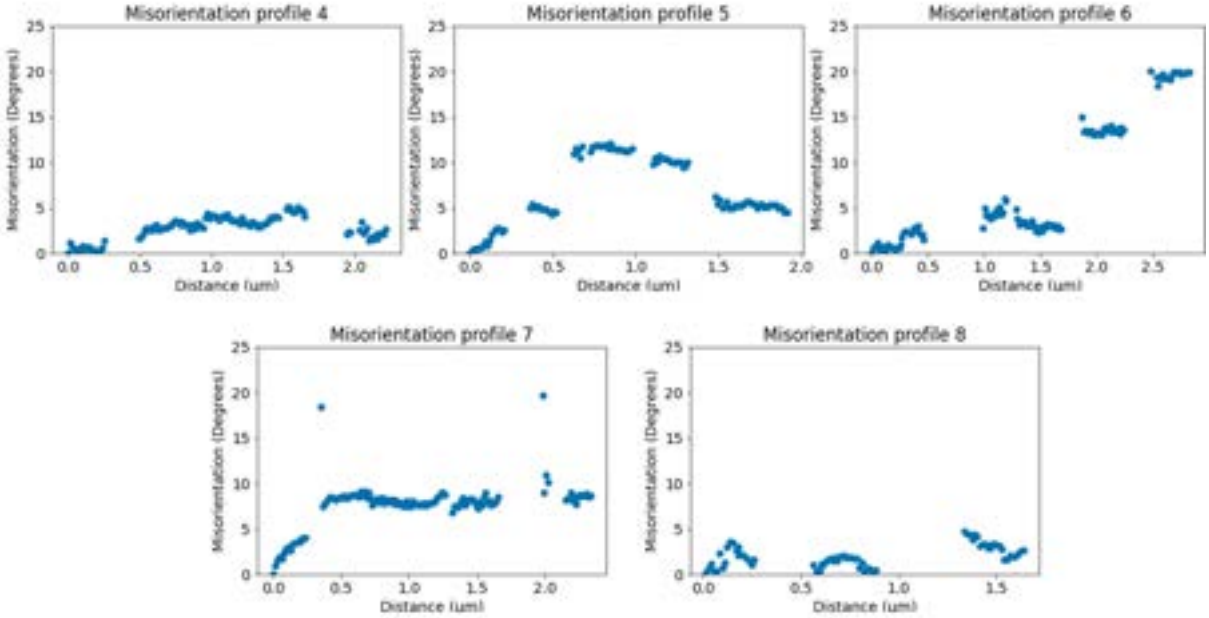

Figure S6: *Misorientation in degrees of line-scan 4 till 8. The noise coming from the gaps between the grains is masked from the plot*

References

[1] UNFCC, "Adoption of the paris agreement."

[2] H.-O. Pörtner, D. Roberts, M. Tignor, E. Poloczanska, K. Mintenbeck, A. Alegría, M. Craig, S. Langsdorf, S. Löschke, V. Möller, A. Okem, and B. R. (eds.), "Climate change 2022: Impacts, adaptation, and vulnerability. contribution of working group ii to the sixth assessment report of the intergovernmental panel on climate change," 2022.

[3] A. Smets, "Solar energy: The physics and engineering of photovoltaic conversion, technologies and systems."

[4] M. J. D. Wild-Scholten, "Energy payback time and carbon footprint of commercial photovoltaic systems," *Solar Energy Materials and Solar Cells*, vol. 119, pp. 296–305, 2013.

[5] S. Philipps, "Photovoltaics report," 2022.

[6] N. G. Park, "Perovskite solar cells: An emerging photovoltaic technology," 3 2015.

[7] L. Schmidt-Mende, V. Dyakonov, S. Olthof, F. Ünlü, K. M. T. Lê, S. Mathur, A. D. Karabanov, D. C. Lupascu, L. M. Herz, A. Hinderhofer, F. Schreiber, A. Chernikov, D. A. Egger, O. Shargaieva, C. Cocchi, E. Unger, M. Saliba, M. M. Byranvand, M. Kroll, F. Nehm, K. Leo, A. Redinger, J. Höcker, T. Kirchartz, J. Warby, E. Gutierrez-Partida, D. Neher, M. Stolterfoht, U. Würfel, M. Unmüssig, J. Herterich, C. Baretzky, J. Mohanraj, M. Thelakkat, C. Maheu, W. Jaegermann, T. Mayer, J. Rieger, T. Fauster, D. Niesner, F. Yang, S. Albrecht, T. Riedl, A. Fakharuddin, M. Vasilopoulou, Y. Vaynzof, D. Moia, J. Maier, M. Franckevičius, V. Gulbinas, R. A. Kerner, L. Zhao, B. P. Rand, N. Glück, T. Bein, F. Matteocci, L. A. Castriotta, A. D. Carlo, M. Scheffler, and C. Draxl, "Roadmap on organic-inorganic hybrid perovskite semiconductors and devices," *APL Materials*, vol. 9, 10 2021.

[8] X. Tian, S. D. Stranks, and F. You, "Life cycle energy use and environmental implications of high-performance perovskite tandem solar cells," 2020.

[9] J. W. Lee, S. H. Bae, N. D. Marco, Y. T. Hsieh, Z. Dai, and Y. Yang, "The role of grain boundaries in perovskite solar cells," 3 2018.

[10] M. A. Green, A. Ho-Baillie, and H. J. Snaith, "The emergence of perovskite solar cells," *Nature photonics*, vol. 8, no. 7, pp. 506–514, 2014.

[11] A. K. Jena, A. Kulkarni, and T. Miyasaka, "Halide perovskite photovoltaics: Background, status, and future prospects," *Chemical Reviews*, vol. 119, pp. 3036–3103, 3 2019.

[12] A. McEvoy, L. Castaner, and T. Markvart, *Solar cells: materials, manufacture and operation*. Academic Press, 2012.

[13] V. E. 105, N. B. Er, and W. P. Dvmkk, "Physical review spontaneous radiative recombination in semiconductors*," 1957.

[14] C. M. Wolff, P. Caprioglio, M. Stolterfoht, and D. Neher, "Nonradiative recombination in perovskite solar cells: The role of interfaces," *Advanced Materials*, vol. 31, 12 2019.

[15] T. S. Sherkar, C. Momblona, L. Gil-Escrig, J. Ávila, M. Sessolo, H. J. Bolink, and L. J. A. Koster, "Recombination in perovskite solar cells: Significance of grain boundaries, interface traps, and defect ions," *ACS Energy Letters*, vol. 2, pp. 1214–1222, 5 2017.

[16] A. Richter, S. W. Glunz, F. Werner, J. Schmidt, and A. Cuevas, "Improved quantitative description of auger recombination in crystalline silicon," *Physical Review B - Condensed Matter and Materials Physics*, vol. 86, 10 2012.

[17] C. M. Proctor, M. Kuik, and T. Q. Nguyen, "Charge carrier recombination in organic solar cells," 12 2013.

[18] S. Jariwala, H. Sun, G. W. Adhyaksa, A. Lof, L. A. Muscarella, B. Ehrler, E. C. Garnett, and D. S. Ginger, "Local crystal misorientation influences non-radiative recombination in halide perovskites," *Joule*, vol. 3, pp. 3048–3060, 12 2019.

[19] W. A. Dunlap-Shohl, Y. Zhou, N. P. Padture, and D. B. Mitzi, "Synthetic approaches for halide perovskite thin films," *Chemical Reviews*, vol. 119, pp. 3193–3295, 3 2019.

[20] J. Anwar and D. Zahn, "Uncovering molecular processes in crystal nucleation and growth by using molecular simulation," 2 2011.

[21] A. M. Ganose, C. N. Savory, and D. O. Scanlon, "Beyond methylammonium lead iodide: prospects for the emergent field of ns2 containing solar absorbers," *Chemical Communications*, vol. 53, pp. 20–44, 2017.

[22] R. Ciesielski, F. Schäfer, N. F. Hartmann, N. Giesbrecht, T. Bein, P. Docampo, and A. Hartschuh, "Grain boundaries act as solid walls for charge carrier diffusion in large crystal mapi thin films," *ACS Applied Materials and Interfaces*, vol. 10, pp. 7974–7981, 3 2018.

[23] O. Shargaieva, F. Lang, J. Rappich, T. Dittrich, M. Klaus, M. Meixner, C. Genzel, and N. H. Nickel, "Influence of the grain size on the properties of ch3nh3pbi3 thin films," *ACS Applied Materials and Interfaces*, vol. 9, pp. 38428–38435, 11 2017.

[24] C. C. Boyd, R. Cheacharoen, T. Leijtens, and M. D. McGehee, "Understanding degradation mechanisms and improving stability of perovskite photovoltaics," 3 2019.

[25] N. Sahu and S. Panigrahi, "Fundamental understanding and modeling of spin coating process : A review," 2009.

[26] M. M. Tavakoli, L. Gu, Y. Gao, C. Reckmeier, J. He, A. L. Rogach, Y. Yao, and Z. Fan, "Fabrication of efficient planar perovskite solar cells using a one-step chemical vapor deposition method," *Scientific Reports*, vol. 5, 9 2015.

[27] C. Tan, J. Chen, X. J. Wu, and H. Zhang, "Epitaxial growth of hybrid nanostructures," *Nature Reviews Materials*, vol. 3, 1 2018.

[28] N. Kaiser, "Review of the fundamentals of thin-film growth," 2002.

[29] "Single-crystal thin films of cesium lead bromide perovskite epitaxially grown on metal oxide perovskite (srtio3)," *Journal of the American Chemical Society*, vol. 139, pp. 13525–13532, 9 2017.

[30] P. S. Whitfield, N. Herron, W. E. Guise, K. Page, Y. Q. Cheng, I. Milas, and M. K. Crawford, "Structures, phase transitions and tricritical behavior of the hybrid perovskite methyl ammonium lead iodide," *Scientific Reports*, vol. 6, 10 2016.

[31] C. Herrero, "Dependence of the silicon lattice constant on isotopic mass," *Solid state communications*, vol. 110, no. 5, pp. 243–246, 1999.

[32] B. K. Patra, H. Agrawal, J. Y. Zheng, X. Zha, A. Travesset, and E. C. Garnett, "Close-packed ultrasmooth self-assembled monolayer of cspbbr3perovskite nanocubes," *ACS Applied Materials and Interfaces*, vol. 12, pp. 31764–31769, 7 2020.

[33] L. Protesescu, S. Yakunin, M. I. Bodnarchuk, F. Krieg, R. Caputo, C. H. Hendon, R. X. Yang, A. Walsh, and M. V. Kovalenko, "Nanocrystals of cesium lead halide perovskites (cspbx3, x= cl, br, and i): novel optoelectronic materials showing bright emission with wide color gamut," *Nano letters*, vol. 15, no. 6, pp. 3692–3696, 2015.

[34] J. Shamsi, A. S. Urban, M. Imran, L. D. Trizio, and L. Manna, "Metal halide perovskite nanocrystals: Synthesis, post-synthesis modifications, and their optical properties," *Chemical Reviews*, vol. 119, pp. 3296–3348, 3 2019.

[35] S. Nasir, M. Z. Hussein, Z. Zainal, N. A. Yusof, S. A. M. Zobir, and I. M. Alibe, "Potential valorization of by-product materials from oil palm: A review of alternative and sustainable carbon sources for carbon-based nanomaterials synthesispotential valorization of by-product materials from oil palm: A review of alternative and sustainable carbon sources for carbon-based nanomaterials synthesis," *BioResources*, vol. 14, pp. 2352–2388, 2 2019.

[36] T. Du, C. H. Burgess, J. Kim, J. Zhang, J. R. Durrant, and M. A. McLachlan, "Formation, location and beneficial role of pbi2 in lead halide perovskite solar cells," *Sustainable Energy and Fuels*, vol. 1, pp. 119–126, 2017.

[37] T. Hellmann, C. Das, T. Abzieher, J. A. Schwenzer, M. Wussler, R. Dachauer, U. W. Paetzold, W. Jaegermann, and T. Mayer, "The electronic structure of mapi-based perovskite solar cells: Detailed band diagram determination by photoemission spectroscopy comparing classical and inverted device stacks," *Advanced Energy Materials*, vol. 10, no. 42, p. 2002129, 2020.

[38] R. Rajeswarapalanichamy, A. Amudhavalli, R. Padmavathy, and K. Iyakutti, "Band gap engineering in halide cubic perovskites cspbbr3- yiy (y= 0, 1, 2, 3)–a dft study," *Materials Science and Engineering: B*, vol. 258, p. 114560, 2020.

[39] J. Qian, B. Xu, and W. Tian, "A comprehensive theoretical study of halide perovskites abx3," *Organic Electronics*, vol. 37, pp. 61–73, 10 2016.